Using functional genetic screens to understand and overcome PARP inhibitor resistance

Paes Lobo Lopes Dias, M.

Citation

Paes Lobo Lopes Dias, M. (2023, January 18). *Using functional genetic screens to understand and overcome PARP inhibitor resistance*. Retrieved from https://hdl.handle.net/1887/3512289

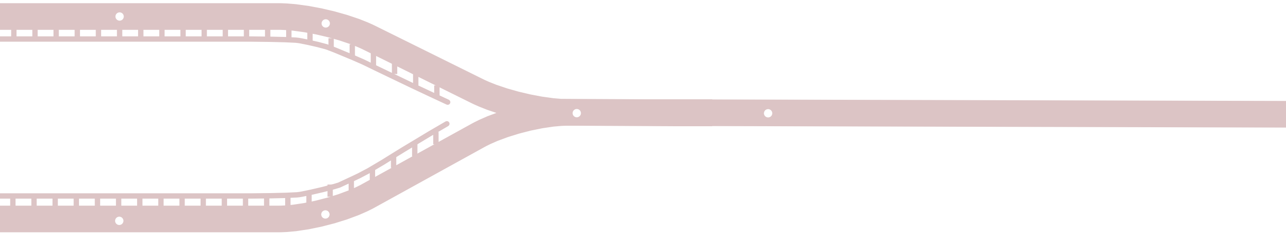

Chapter 3

Multi-omics analysis reveals distinct non-reversion mechanisms of PARPi resistance in BRCA1- versus BRCA2-deficient mammary tumors

Jinhyuk Bhin*, Mariana Paes Dias*, Ewa Gogola*, Frank Rolfs, Sander R. Piersma, Roebi de Bruijn, Julian R. de Ruiter, Bram van den Broek, Alexandra A. Duarte, Wendy Sol, Ingrid van der Heijden, Lara Bakker, Taina S. Kaiponen, Cor Lieftink, Ben Morris, Roderick L. Beijersbergen, Marieke van de Ven, Connie R. Jimenez, Lodewyk F. A. Wessels, Sven Rottenberg and Jos Jonkers

*equal contribution

Submitted, BioRxiv, 2022; 2022.09.07.506927

ABSTRACT

BRCA1 and BRCA2 both function in DNA double-strand break repair by homologous recombination (HR). Due to their HR-defect, BRCA1/2-deficient cancers are sensitive to poly(ADP-ribose) polymerase inhibitors (PARPi) but they eventually acquire resistance. Preclinical studies yielded several PARPi resistance mechanisms that do not involve BRCA1/2 reactivation, but their relevance in the clinic remains elusive. To investigate which BRCA1/2-independent mechanisms drive spontaneous resistance in vivo, we combined molecular profiling with functional analysis of the HR status of matched PARPi-naïve and PARPi-resistant mouse mammary tumors harboring large intragenic deletions that prevent functional restoration of BRCA1/2. We observed restoration of HR in 64% of PARPi-resistant BRCA1-deficient tumors but none in the PARPi-resistant BRCA2-deficient tumors. Moreover, we found that 53BP1 loss is the prevalent resistance mechanism in HR-proficient BRCA1-deficient tumors, whereas resistance in BRCA2-deficient tumors is mainly induced by the loss of PARG. Our combined multi-omics analysis catalogued additional genes and pathways potentially involved in modulating PARPi response.

INTRODUCTION

The observation that many oncogenic events render cancer cells reliant on specific and druggable biological pathways is a premise of targeted therapies for personalized cancer treatment. Unfortunately, the selective pressure that initially kills cancer cells is also a driving force in selecting cells which acquired drug resistance. A better understanding of the recurrent molecular patterns of resistance in specific genetic contexts is therefore instrumental to improve clinical outcomes.

One example of cancer dependencies that can be exploited therapeutically is the defect in the repair of DNA double-strand breaks (DSBs) through homologous recombination (HR) due to BRCA1 or BRCA2 inactivation[1,2]. Unlike the other DSB repair pathways, HR enables the accurate repair of DNA lesions as it uses the newly replicated sister chromatid as a template. Both BRCA1 and BRCA2 are essential in this process. While BRCA1 is required for the initiation of HR by promoting end-resection of the DSB, BRCA2 acts further downstream and, together with PALB2, stimulates the recruitment of RAD51 recombinase to the resected single-stranded DNA[3]. The HR defect resulting from the loss of BRCA1/2 can be targeted through the inhibition of poly(ADP-ribose) polymerase (PARP) enzymes PARP1 and PARP2[1,2]. PARP1/2 have been implicated in several DNA damage response (DDR) pathways, including the repair of DNA single strand breaks (SSBs), DSBs and stabilization of replication forks (RFs)[4]. Catalytic inhibition as well as trapping of PARP1/2 on the DNA by PARP inhibitors (PARPi) leads to replication-coupled DSBs formation, which in turn requires HR for error-free repair[5]. BRCA1/2-defective cells can only employ error-prone repair to resolve the DSBs caused by PARPi treatment, resulting in accumulation of chromosomal aberrations and cell death by mitotic catastrophe[6]. The success of this approach resulted in the clinical approval of four different PARPi for the treatment of several types of cancers with HR defects[7].

Despite the clinical benefit, sustained antitumor responses to PARPi are often hampered by the emergence of resistance. Previous studies have delineated several mechanisms by which BRCA1/2-deficient tumors evade PARPi toxicity[7]. Independently of HR, PARPi resistance may be induced through (i) cellular extrusion of PARPi by upregulation of the drug efflux transporter P-gp[8]; (ii) partial restoration of catalytic PARP activity through loss of poly(ADP-ribose) glycohydrolase (PARG)[9]; (iii) PARP1 downregulation/inactivation as well as mutations that abolish PARP1 trapping[5,10,11]; and (iv) restoration of RF stability[12–14]. All these mechanisms result in PARPi resistance by limiting PARPi-induced DNA damage, rather than restoring the capacity of BRCA1/2-deficient cells to efficiently repair DSBs. In contrast, HR restoration as result of secondary (epi)genetic events that lead to reactivation of functional BRCA1/2 may fully cancel the initial susceptibility to PARPi. In addition, genetic screens and *in vivo* studies in preclinical models demonstrated that inactivation of the 53BP1-RIF1-shieldin DSB end-protection pathway, which inhibits HR and is antagonized by BRCA1 during S phase, partially restores HR and confers PARPi resistance in BRCA1-deficient cells[15–30].

While multiple mechanisms of acquired PARPi resistance have been reported in preclinical *in vitro* models, their clinical relevance remains unclear. To date, the best clinically documented mechanism of resistance is restoration of BRCA1/2 function by secondary (epi)genetic events (e.g., reversion mutations)[31]. However, these results might be biased by the fact that PARPi were initially approved for second-line maintenance therapy following first-line treatment with platinum- based chemotherapies. Since (epi)genetic reactivation of BRCA1/2 function has been shown to be the main mechanism of platinum resistance in *BRCA1/2*-mutated tumors, it is plausible that some of these patients might have already developed BRCA-proficient, and therefore PARPi-resistant, tumor clones as a result of a first-line treatment[32–35]. Moreover, reactivation of BRCA1/2 function is not found in all patients with refractory tumors[33,36], suggesting that BRCA1/2-independent PARPi resistance is relevant in the clinic.

The PARPi olaparib and niraparib have recently been approved as first-line maintenance therapies and clinical trials have started to test PARPi as single-agent neoadjuvant therapy[37]. With more patients likely to receive PARPi earlier in the course of disease, it is important to understand which are the most frequent mechanisms of acquired PARPi resistance, and if these differ between *BRCA1*- and *BRCA2*-mutated tumors, in order to predict PARPi response and to develop strategies to overcome resistance. In the absence of available clinical data, we sought to answer these questions by combining functional analysis of HR status with molecular profiling of a unique collection of matched PARPi-naïve and PARPi-resistant mouse mammary tumors which harbor large intragenic deletions of *Brca1* or *Brca2* genes that cannot be spontaneously restored. Overall, our study shows that functional differences between BRCA1 and BRCA2 in the repair of DSBs also impact the resistance patterns in PARPi-treated tumors. While HR restoration accounted for the majority of BRCA1-deficient tumors, it did not occur in BRCA2-deficient tumors, suggesting that HR cannot be restored in *Brca2*-mutated tumors that cannot undergo BRCA2 reactivation. Moreover, among the previously reported resistance mechanisms, loss of 53BP1 and loss of PARG were the most dominant alterations in PARPi-resistant BRCA1-deficient and BRCA2-deficient tumors, respectively. Dysregulation of other known resistance factors was only sporadically observed, suggesting 53BP1 and PARG as potential biomarkers of acquired PARPi resistance. Additionally, our analysis yielded a list of potential genes and pathways involved in PARPi response and provides evidence that tumor-intrinsic alterations in pathways regulating the tumor microenvironment may influence PARPi efficacy.

RESULTS

HR restoration drives PARPi resistance in BRCA1-deficient tumors

To study the contribution of BRCA1/2-independent PARPi resistance mechanisms in BRCA1/2-deficient tumors, we used two genetically engineered mouse models (GEMMs) of BRCA1-associated breast cancer, *K14cre;Brca1*$^{F/F}$*;Trp53*$^{F/F}$ (KB1P) and *K14cre;Brca1*$^{F/}$

^{F};*Trp53*$^{F/F}$;*Mdr1a/b*$^{-/-}$ (KB1PM) as well as a GEMM of BRCA2-associated breast cancer, *K14cre;Brca2*$^{F/F}$;*Trp53*$^{F/F}$ (KB2P)[8,9,38–40] (**Fig. 1A**). In these models, long-term treatment of mammary tumors with PARPi leads to spontaneous induction of resistance, which is preserved upon tumor passaging[38,41]. Importantly, the tumors arising in these models harbor large intragenic deletions in the *Brca1* or *Brca2* genes[39,40] and thus resistance to PARPi cannot be acquired via reactivation of BRCA1/2 function. Moreover, we eliminated the possibility of P-glycoprotein (Pgp)-mediated resistance to the PARPi olaparib by either the genetic inactivation of Pgp (*Mdr1a/b*) in the KB1PM model, or by treating Pgp-proficient KB1P and KB2P tumors with the PARPi AZD2461, which is a poor substrate for this transporter[38,42] (**Fig. 1A**).

HR deficiency is the basis for sensitivity to PARPi and thus we hypothesized that HR restoration is the most likely way for tumors to acquire resistance to PARPi. We therefore assessed the HR status of matched PARPi-naïve and PARPi-resistant tumors by measuring their capacity to form ionizing radiation-induced RAD51 foci (RAD51-IRIF)[23,43] (**Fig. 1B**). As a positive control for this assay, we used a HR-proficient mammary tumor derived from the *K14cre;Trp53*$^{F/F}$ (KP) model and observed the highest accumulation of RAD51 foci 2 hours after induction of DNA damage (**Supplementary Fig. 1A-D.**). Of note, all tumors exhibited high growth rates prior to irradiation, suggesting that differences in cell cycle distribution between the samples are negligible (**Supplementary Fig. 1E,F**). As expected, we did not detect any RAD51-IRIF formation in any of the PARPi-naïve tumors (**Fig. 1C,D**), confirming that the *Brca1/2* deletions induced in our models completely abolish HR-mediated repair. Consistent with this, whole-exome sequencing of DNA from PARPi-resistant tumors confirmed the complete Cre-mediated deletion of the floxed *Brca1/2* exons, thus no emerging resistance could be attributed to the selection of clones that retained wild-type BRCA proteins (**Supplementary Fig. 1G,H**). Analysis of the 45 PARPi-resistant BRCA1-deficient (BRCA1-KO) tumors revealed that 64% (29/45) of the tumors had restored the capacity to form RAD51 foci, including one tumor with a mixed pattern (RAD51-IRIF positive and negative areas) (**Fig. 1E**). These results indicate that HR recovery is the predominant mechanism of PARPi resistance in the KB1P(M) models, albeit not the only one. In contrast, none of the 26 PARPi-resistant BRCA2-deficient tumors exhibited RAD51-IRIF (**Fig. 1E**)[9]. Given that PARPi treatment is a potent trigger of HR restoration in the KB1P(M) models, lack of RAD51-IRIF in the BRCA2-deficient cohort strongly indicates that BRCA2 is indispensable for HR repair.

Alterations in previously reported PARPi resistance factors

To understand how prolonged PARPi treatment reshapes BRCA1/2-deficient tumors, we performed whole-exome sequencing (WE-seq), low-coverage whole-genome sequencing (LCWG-seq), and RNA sequencing (RNA-seq) on the collection of matched PARPi-naïve and PARPi-resistant KB1P(M) and KB2P tumors and identified alterations specific to each resistant tumor compared to the matched naïve tumor.

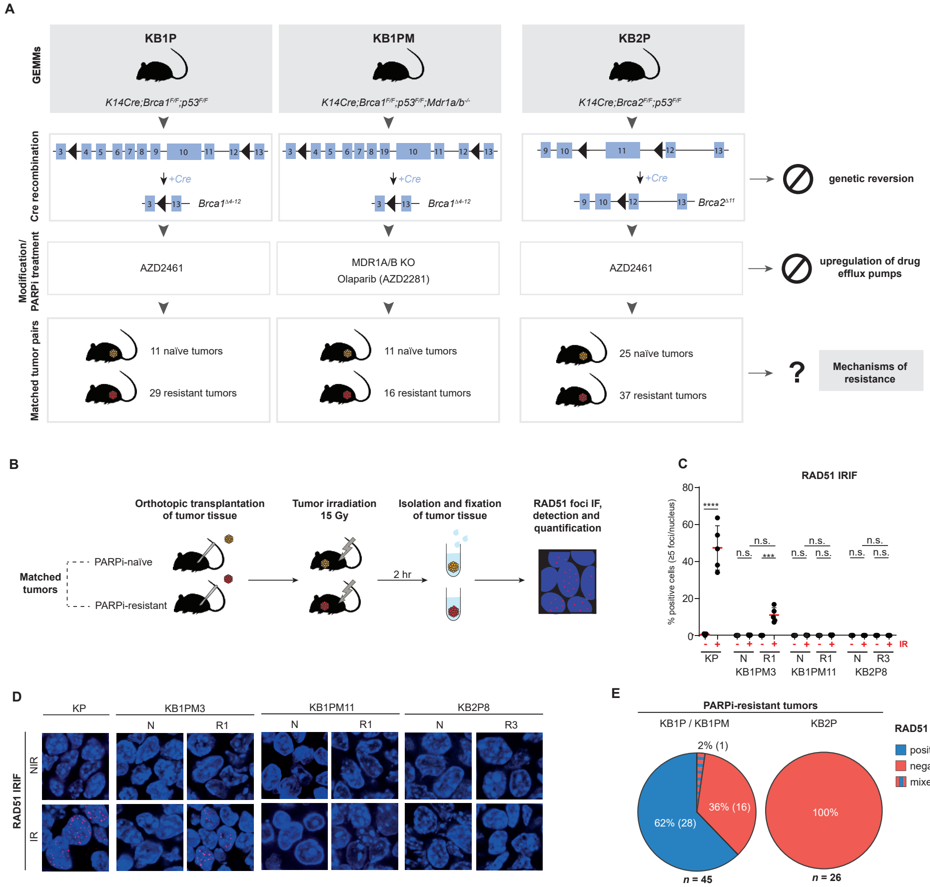

Figure 1 | HR restoration drives PARPi resistance in BRCA1-deficient tumors. A | Outline of the generation of matched PARPi-naive and PARPi-resistant KB1P(M) and KB2P tumors and of the experimental approach. **B |** Schematic representation of the RAD51 IRIF formation assay. Cryopreserved PARPi-naïve and PARPi-resistant tumors were orthotopically transplanted into syngeneic recipient mice and, upon outgrowth to 500 mm3, DNA damage was inflicted by locally applied ionizing radiation (IR) at a dose of 15Gy. 2hr post-irradiation, tumors were isolated and fixed tissues were used for RAD51 immunofluorescence imaging. **C-D |** Quantification (C) and representative images (D) of the RAD51 IRIFs for the different matched KB1P(M) and KB2P tumor pairs and control KP tumors; IR – irradiated, NIR – non irradiated; scale bar, 100 μm; data in (C) represented as percentage of positive cells (≥5 foci/nucleus) per imaged area (single data point, typically 100-200 cells/area); ****p<0.0001, ***p<0.001, ** p<0.01 (two-tailed Mann-Whitney U test). **E |** Pie charts showing the outcome of the RAD51 IRIF assay in PARPi-resistant KB1P(M) and KB2P tumor cohorts; percentages and numbers of individual tumors analyzed are indicated; n – total number of individual tumors analyzed from the indicated models. p=0.0001 (two-tailed Fisher's exact test).

We first interrogated if we could find genetic and transcriptional alterations in factors previously associated with PARPi resistance (**Fig. 2A**). To this end, we selected 25 genes reported to drive PARPi resistance due to BRCA-independent HR restoration, restoration of fork stability or modulation of PARP signaling/trapping[7] (**Supplementary table 1**). We examined alterations in these genes in the different PARPi-resistant tumor groups with informed HR status, i.e., (1) RAD51-positive KB1P(M), (2) RAD51-negative KB1P(M) and (3) KB2P tumors. Of the 25 genes, 23 have been reported to drive PARPi resistance upon loss of function, whereas 2 genes drive resistance as a result of gain of function. Globally, we found alterations in all known factors analyzed, which occurred at different frequencies in the different PARPi-resistant tumor groups. Nearly eighty percent (55/71) of all resistant tumors harbored deleterious mutations, copy number variations, and/or gene expression changes in at least one known factor. *Shld2*, *Parg*, *Rif1*, *Trp53bp1*, *Rev7*, *Ezh2*, *Mre11a*, *Mll3* and *Mll4* were amongst the most frequently altered genes (≥10% of all tumors) (**Fig. 2A**).

We next asked whether certain genes were preferentially altered within the three different PARPi-resistant tumor groups. We found that *Trp53bp1*, one of the best-studied PARPi-resistance factors involved in HR restoration via loss of DSB end-protection, was specifically altered in RAD51-positive KB1P(M) tumors (41%) as compared to RAD51-negative KB1P(M) (7%) and KB2P (3%) tumors (**Fig. 2A-D**). In contrast, *Shld2* and *Parg* were preferentially altered by copy number loss in KB2P tumors compared to KB1P(M) tumors (**Fig. 2A,C**). Previously, we reported that loss of PARG causes PARPi resistance independently of BRCA1/2 by restoring PAR formation and restoring the recruitment of DNA repair factors downstream of PARP1[9]. While we expected *Parg* to be equally altered in both KB1P(M) and KB2P tumors, we found that *Parg* was more frequently lost in KB2P tumors (44%) (**Fig. 2A,C**) than in RAD51-positive (18%) and RAD51-negative KB1P(M) tumors (27%) (**Fig. 2B**). The genomic location of *Shld2* is proximal to *Parg* (chr14qB) and thus copy number loss of *Parg* is often accompanied by concomitant loss of *Shld2* (**Fig. 2A**). Moreover, depletion of SHLD2 has been reported to drive PARPi resistance via HR restoration in BRCA1-deficient cells but not in BRCA2-deficient cells. Hence, loss of *Shld2* in KB2P tumors is most likely a consequence of *Parg* copy number loss rather than driving resistance to PARPi. In support of this, CRISPR/Cas9-mediated inactivation of SHLD2 did not drive resistance in cultured KB2P tumor cells (**Supplementary Fig. 2A,B**). MRE11 downregulation or copy loss was only found in KB2P and RAD51-negative KB1P(M) tumors, suggesting MRE11 is specifically lost in RAD51-negative PARPi-resistant tumors (**Fig. 2A,D**). This is in line with its key role in HR and suggests that loss of MRE11 may induce PARPi resistance by promoting RF protection.

We also applied Detection of Imbalanced Differential Signal (DIDS) analysis specifically designed for the detection of subgroup markers in heterogeneous populations[44]. This tool is particularly useful for identifying drug resistance factors in a tumor group with multiple resistance mechanisms by detecting genes with outlying expression in the subset of resistant tumors compared to all naïve tumors[9,45]. DIDS analysis additionally identified *Rev7* to be significantly downregulated in RAD51-positive PARPi-resistant KB1P(M) tumors, which is consistent with its role in the 53BP1-RIF1-shieldin pathway involved in DSB end-protection, and with the observation that REV7 loss promotes HR and PARPi resistance in BRCA1-deficient cells[17,18,23,24,30] (**Fig. 2E,F**). *Ezh2*, which was previously shown to promote fork stability and PARPi resistance when depleted, was also identified by DIDS analysis to be downregulated in PARPi-resistant KB2P tumors, in accordance with the previous findings that loss of EZH2 impairs response to PARPi in BRCA2-deficient cells but not in BRCA1-deficient cells[46] (**Fig. 2E,G**). Surprisingly, *Rif1* was significantly downregulated in PARPi-resistant KB2P tumors, suggesting RIF1 might have 53BP1-RIF1-shieldin-independent functions that could drive resistance in BRCA2-deficient tumors (**Fig. 2E,H**).

To confirm that PARPi resistance mediated by 53BP1 loss is enriched in RAD51-positive PARPi-resistant tumors, we evaluated the functional impairment of 53BP1 in KB1P(M) and KB2P tumors by analyzing 53BP1-IRIF formation (**Supplementary Fig. 2C,D**). We found that loss of 53BP1-IRIF was only detected in RAD51-positive or mixed PARPi-resistant KB1P(M) tumors, whereas PARPi-resistant KB2P tumors as well as PARPi-naïve KB1P(M) or KB2P tumors did not show loss of 53BP1-IRIF (**Fig. 2I and Supplementary Fig. 2E**). Consistently, tumors with loss of 53BP1-IRIF showed lower *Trp53bp1* expression levels than other tumors, suggesting good concordance between the omics data and the functional assay (**Fig. 2J**). Altogether, our analysis revealed multiple known factors significantly altered in RAD51-positive KB1P(M) and in KB2P tumors; however, none were found to specifically explain PARPi resistance in RAD51-negative PARPi-resistant KB1P(M) tumors.

HR-deficient PARPi-resistant BRCA1-KO tumors show increased immune cell infiltration

We then systematically characterized the three resistant tumor groups beyond the known resistance factors using our genomic and transcriptomics data. To identify recurrent focal genomic alterations between resistant and matched naïve tumors, we performed copy number analysis using RUBIC[47]. The majority of the significantly recurrent alterations identified in PARPi-resistant tumors were focal deletions (**Supplementary Fig. 3A-C**), including loss of the regions encoding *Rev7* in RAD51-positive KB1P(M) tumors and *Parg* in KB2P tumors, respectively (**Supplementary Fig. 3A, C**). In PARPi-resistant RAD51-negative KB1P(M) tumors, we could not identify recurrent focal events, with the exception of one amplified locus on chromosome 8 (**Supplementary Fig. 3B**). Several genes encoded within the recurrently amplified/deleted loci in PARPi-resistant KB1P(M) and KB2P tumors are associated with DDR pathways (**Supplementary Fig. 3D**). Gene set analysis (GSA) demonstrated that genes involved in cell cycle/proliferation were depleted in PARPi-resistant RAD51-positive KB1P(M) tumors, whereas genes involved in positive regulation of immune cell activation were amplified in PARPi-resistant RAD51-negative KB1P(M) tumors (**Supplementary Fig. 3E-G**).

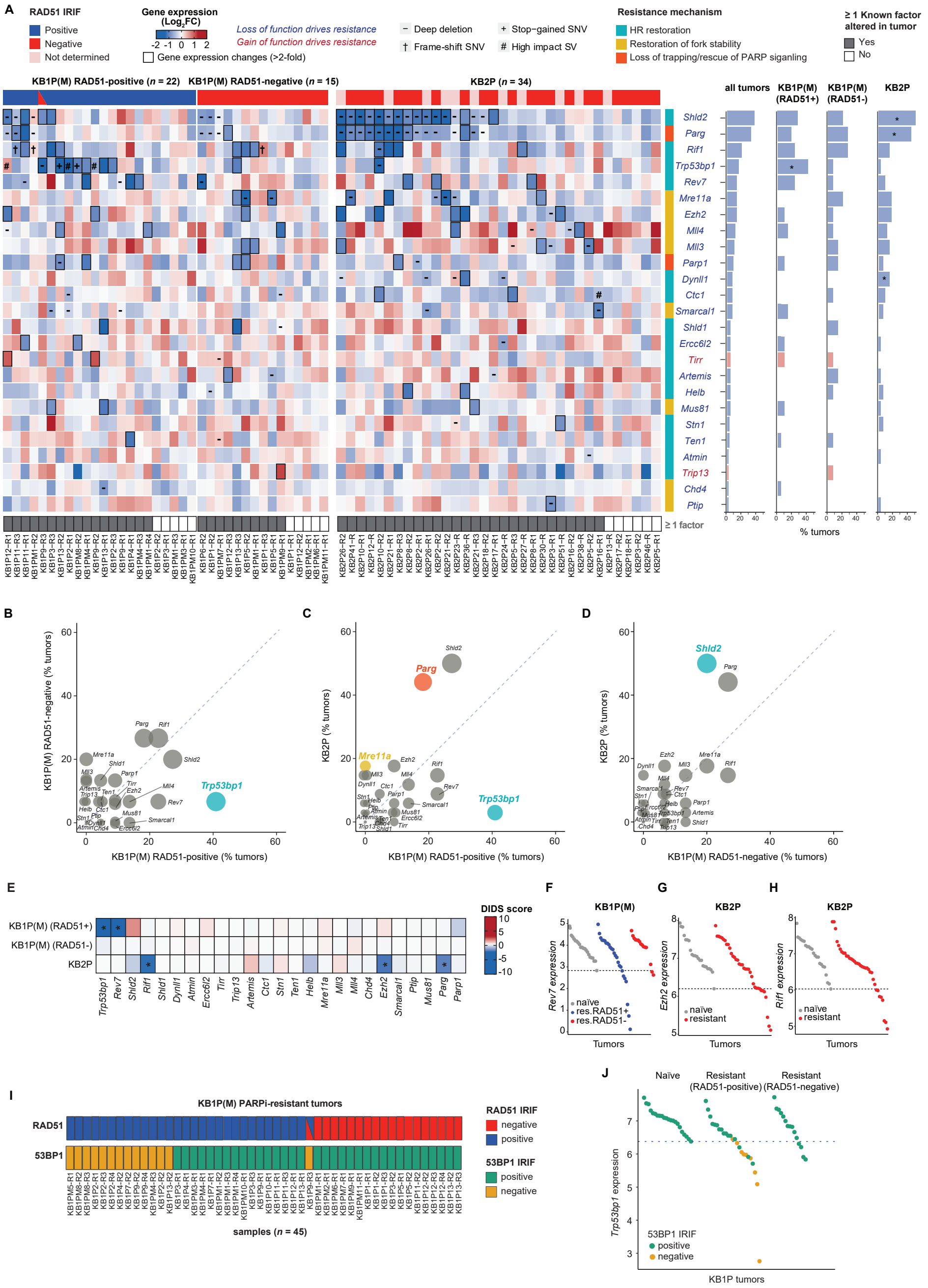

Figure 2 | Alterations in previously reported PARPi resistance factors. A | Heatmap (left) of gene expression changes between matched resistant vs naïve KB1P(M) and KB2P tumors for the previously reported PARPi resistance genes 7. Genes for which loss or gain of function have been reported to drive resistance are indicated in blue or red, respectively. In the heatmap, genomic are marked by different symbols (-: copy number deletion, +: stop-gained SNV, †: frame-shift SNV, #: loss of function SV). The resistant tumors with transcriptional alterations (lower or higher than 2-fold compared to matched naïve tumors for each loss or gain of function drivers) are marked by thicker borderlines. The top panel of the heatmap indicates RAD51 IRIF status which is a proxy for HR status (positive - blue, negative - red, tumors with both positive and negative area - blue and red, tumors for which RAD51 IRIF was not determined, even though expected to be negative - pink). The bottom panel of the heatmap indicates the tumors with alterations in at least one known gene. Resistance mechanisms associated with each gene are categorized by different color bars (light green - HR restoration, purple – restoration of fork stability, light blue – PARP signaling). Frequencies for dysregulation of each gene (by either genomic or transcriptional alterations) are shown in the bar plots next to the heatmap (right). The genes preferentially altered in specific tumor types were assessed by the Fisher's exact test (asterisk, $P<0.05$). **B-D |** Scatter plots comparing the alteration frequency of each PARPi resistance factor in the different resistant tumor types. The size of the circle is proportional to the sum of the alteration frequency of the two resistant tumor types compared and circles are colored if statistically significant (Fisher's exact test, $P<0.05$). The color of the circle indicates the resistance mechanism associated with each resistance factor as mentioned in Figure 2A. **E |** DIDS outlier scores computed from gene expression data for known resistance factors. Red (positive score) and blue (negative score) indicate upregulation and downregulation of each factor in subset of resistant tumors compared to naïve tumors. The genes with significant DIDS scores are marked with asterisk (Permutation-based exact test, $P<0.05$). **F-H |** Dot plots of *Rev7* gene expression in KB1P(M) tumors (F) and *Ezh2* (G) and *Rif1* (H) gene expressions in KB2P tumors where significant DIDS scores were detected. I | RAD51 and 53BP1 IRIF status in KB1P(M) PARPi-resistant tumors measured by in situ IRIF assay. J | Dot plots of *Trp53bp1* gene expression in KB1P(M) tumors with 53BP1 IRIF status.

Next, we transcriptionally characterized the different PARPi-resistant tumor groups. Differential gene expression analysis by limma[48] between resistant and naïve tumors identified 26, 349 and 1058 genes in PARPi-resistant RAD51-positive KB1P(M), RAD51-negative KB1P(M) and KB2P tumors, respectively, including downregulation of *Trp53bp1*, *Parg* and *Shld2* (**Fig. 2A and Supplementary Fig. 3H-J**). No known resistance-associated factors were found to be differentially expressed in RAD51-negative KB1P(M) tumors (**Supplementary Fig. 3I**). GSA of the differentially expressed genes (DEGs) in each group of resistant tumors identified distinct sets of pathways. Interestingly, PARPi-resistant RAD51-negative KB1P(M) tumors showed upregulation of immune-related pathways, including antigen processing and presentation, T-cell receptor signaling and phagosome (**Fig. 3A**), which might be associated with the enrichment of immune cell regulators with focal amplification in these tumors (**Supplementary Fig. 3F**). Co-functionality network analysis of upregulated immune-associated genes using the GeneICA-Network framework [49] revealed several immune cell modules, such as T cells (e.g., CD3D, CD3G, CD247), B cells (e.g., CD22, CD72, CD79A) and antigen presentation (e.g., CD74, CIITA, H2-OB, H2-AA, H2-AB1, H2-EB1, H2DMA, H2-DMB1, H2-DMB2), suggesting an increase in immune cell infiltration (**Fig. 3B**). We validated these findings by carrying out immunohistochemical (IHC) analysis of markers of leucocytes (CD45), T cells (CD3), B cells (B220) and macrophages(F4/80), revealing increased expression of all these markers in PARPi-resistant KB1P(M) tumors when compared to naïve tumors, with RAD51-negative KB1P(M) tumors displaying a stronger increase compared to RAD51-positive KB1P(M) tumors (**Fig. 3C**). Therefore, our findings suggest that RAD51-negative PARPi-resistant KB1P(M) tumors have higher immune infiltration compared to PARPi-naïve and RAD51-positive PARPi-resistant KB1P(M) tumors. Altogether, these data demonstrate that PARPi-resistant tumors display distinct genomic and transcriptomic features depending on BRCA1/2 loss and HR status.

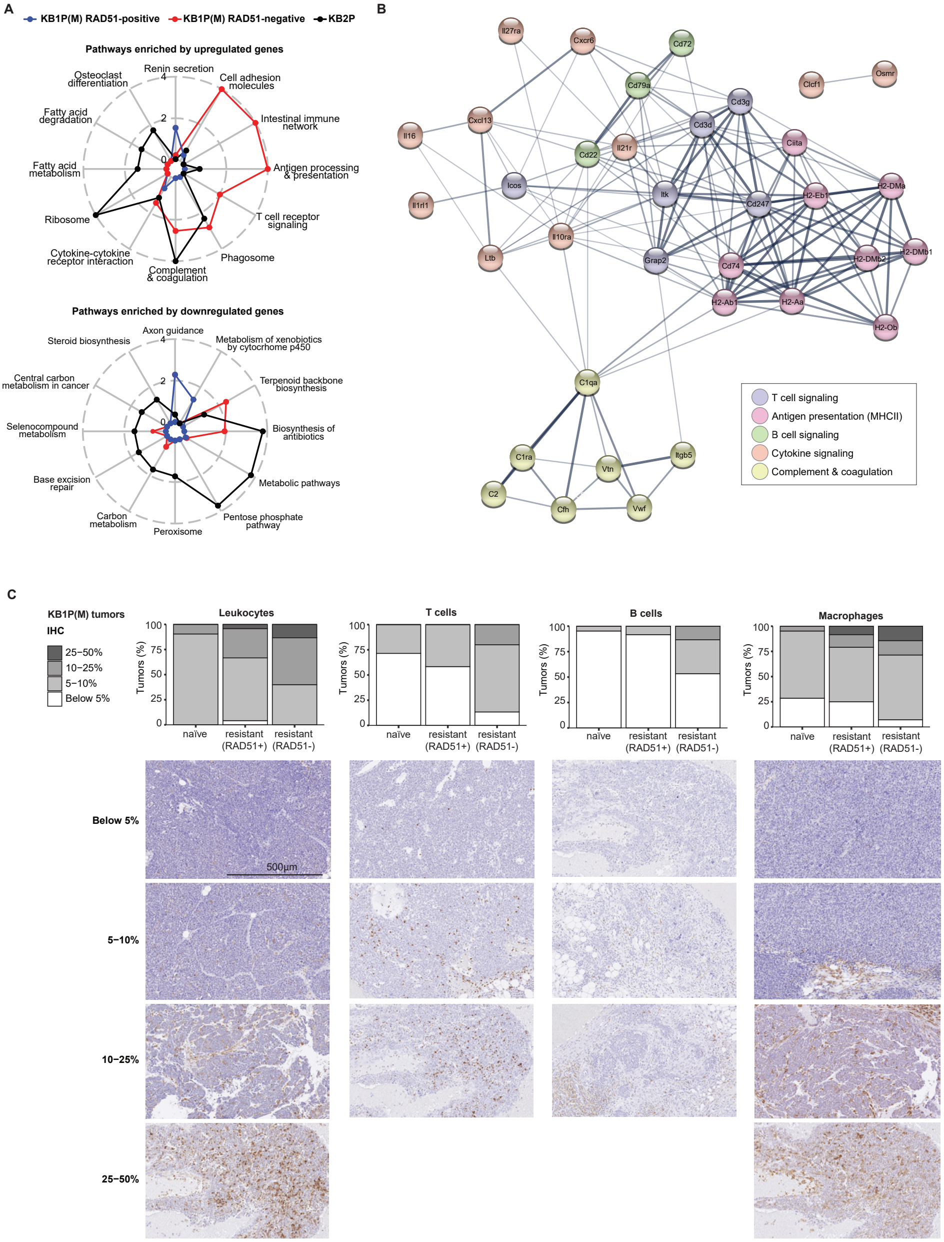

Figure 3 | HR-deficient PARPi-resistant BRCA1-KO tumors show increased immune cell infiltration. A | Radar chart showing pathways enriched by upregulated and downregulated genes in KB1P(M) and KB2P resistant tumors compared to naïve tumors based on gene expression data. **B |** Co-functionality network constructed by STRING [62] for the immune-related genes that are significantly upregulated in RAD51-negative KB1P(M) resistant tumors compared to naive tumors. The genes in the network were annotated by KEGG[62] and colored depending on the annotated pathways. **C |** Quantification and representative images of IHC analysis of markers for different immune cells including leukocytes (CD45), T-cells (CD3), B-cells (B220), and macrophages (F4/80) in KB1P(M) tumors.

Multi-omics analysis identifies potential PARPi-resistance factors/pathways

To catalogue potential PARPi resistance factors, we identified genes displaying resistance-specific genomic (SNVs, INDELs, SVs, focal amplifications/deletions) and transcriptional (DEG sets) alterations in each group of resistant tumors by integrating WE-seq, LCWG-seq and RNA-seq data (**Fig. 4A**). Of note, we extended DEG sets to capture the genes with both homogeneous (by limma) and heterogenous behavior (by DIDS) between naïve and resistant tumors. Overall, we observed limited overlap between genomic and transcriptional alterations across all tumor groups, including several genes involved in DDR (**Fig. 4B and supplementary table 2**). Moreover, the overlap between genomic and transcriptional alterations was mostly derived from copy number alterations, with the exception of *Trp53bp1*, in which we found truncating SNVs and deleterious SVs leading to nonsense-mediated decay. The limited overlap between genomic and transcriptional alterations indicates that the genomic alterations do not always lead to gene expression changes. Nonetheless, several known resistance factors including *Trp53bp1*, *Rev7*, and *Parg* displayed both genomic and transcriptional alterations. We next explored biological pathways represented by the identified genes with resistance-specific genomic and transcriptional alterations (**Fig. 4C and supplementary table 3**). As described before, we found transcriptional upregulation of immune-associated pathways specifically in RAD51-negative KB1P(M) tumors, including upregulation of antigen processing and presentation, B and T cell receptor signaling, as well as immune checkpoint pathways (**Fig. 4C,D**). Interestingly, pathways associated with cell adhesion molecules and ECM-receptor interaction were transcriptionally downregulated in RAD51-positive KB1P(M) tumors, but upregulated in RAD51-negative KB1P(M) tumors (**Fig. 4C,D**). At the genomic level, loss-of-function alterations (mainly copy number loss or deleterious SNVs/SVs) were observed in pathways associated with signaling processes such calcium and cAMP signaling pathways in RAD51-positive KB1P(M) tumors, and in metabolic pathways such as inositol phosphate and carbon metabolism in KB2P tumors (**Figures 4C and 4D**). In line with the limited overlap between genomic and transcriptional alterations (**Fig. 4B**), pathways enriched by genes with genomic alterations showed very limited overlap with those enriched in transcriptional alterations, with the exception of the phagosome pathway (**Fig. 4C**). Nonetheless, we found 46 genes that carried either genomic or transcriptional alterations in all three resistant tumor groups, including 8 genes (*Parp3*, *Gstm1*, *Il18*, *Padi4*, *Dnmt3b*, *Psrc1*, *Rif1* and *Ankrd26*) involved in DDR (**Fig. 4E,F**). Taken together, integration of genomics and transcriptomics data from PARPi-resistant versus PARPi-naïve tumors allowed us to catalogue genes and pathways potentially involved in modulating PARPi response.

To prioritize candidate resistance drivers, we identified genes with genomic alterations that had a significant impact on transcriptional changes in the protein-protein interaction network by carrying out driver analysis with DriverNet[50]. We identified drivers in 25% of genes with resistance-specific mutations and in 23% of genes with copy number alterations (**Supplementary Fig. 4A**). Interestingly, DDR genes were more enriched in drivers compared to non-drivers in all PARPi-resistant tumor groups, with the exception of drivers that were derived from copy number alterations in RAD51-negative KB1P(M) tumors (**Supplementary Fig. 4B-D**), supporting the previous findings that DDR pathways are strongly involved in governing PARPi response[7].

In vitro loss-of-function screens fail to validate candidate drivers of *in vivo* PARPi resistance

To identify causative drivers among the genes associated with PARPi resistance in KB1P(M) tumors, we performed functional genetic enrichment screens in human BRCA1-deficient cell lines. To obtain a comprehensive set of genes to be functionally tested in the screens, we generated global proteomics and phosphoproteomics data and identified proteins (DE-Prot) and phosphoproteins (DE-Phos) that were differentially expressed between naïve and resistant tumors. We combined the DE-Prot and DE-Phos with genes identified from WE-seq, LCWG-seq and RNA-seq analysis for all KB1P(M) tumors, including tumors whose RAD51-IRIF status was not determined, resulting in 3727 resistance-associated genes (**Supplementary Fig. 4E**). Plausible drivers were prioritized by recurrences in multiple datasets, associations with DDR, and potential as network drivers, yielding a final list of 891 putative PARPi resistance driving factors including 53BP1, REV7, HELB and PARG (**Supplementary Fig. 4F**).

We then generated a focused lentiviral shRNA library targeting the identified 891 candidate genes plus 133 non-essential genes as controls (**Supplementary table 5**). Given the strong effect of 53BP1 loss on PARPi resistance, we decided to exclude *Trp53bp1*-targeting shRNAs from the library to prevent them from obscuring less dominant hits. We introduced the lentiviral shRNA library in the human BRCA1-deficient cell lines SUM149PT and RPE1-hTERT-*BRCA1*$^{-/-}$;*TP53*$^{-/-}$, which were subsequently selected with olaparib for three weeks (**Supplementary Fig. 4G**). REV7 behaved as a positive control and was identified as top hit in both cell lines, but no other common hits were found (**Supplementary Fig. 4H,I**). We identified RBMS1 as a hit in the screen carried out in SUM149PT cells (**Supplementary Fig. 4H**), but shRNA-mediated depletion of RBMS1 *in vivo* did not significantly affect survival of KB1P tumor-bearing mice (**Supplementary Fig. 4J**). Overall, these results suggest *in vitro* loss-of-function screens are insufficient to validate the candidate drivers of in vivo PARPi resistance arising from the multi-omics analysis.

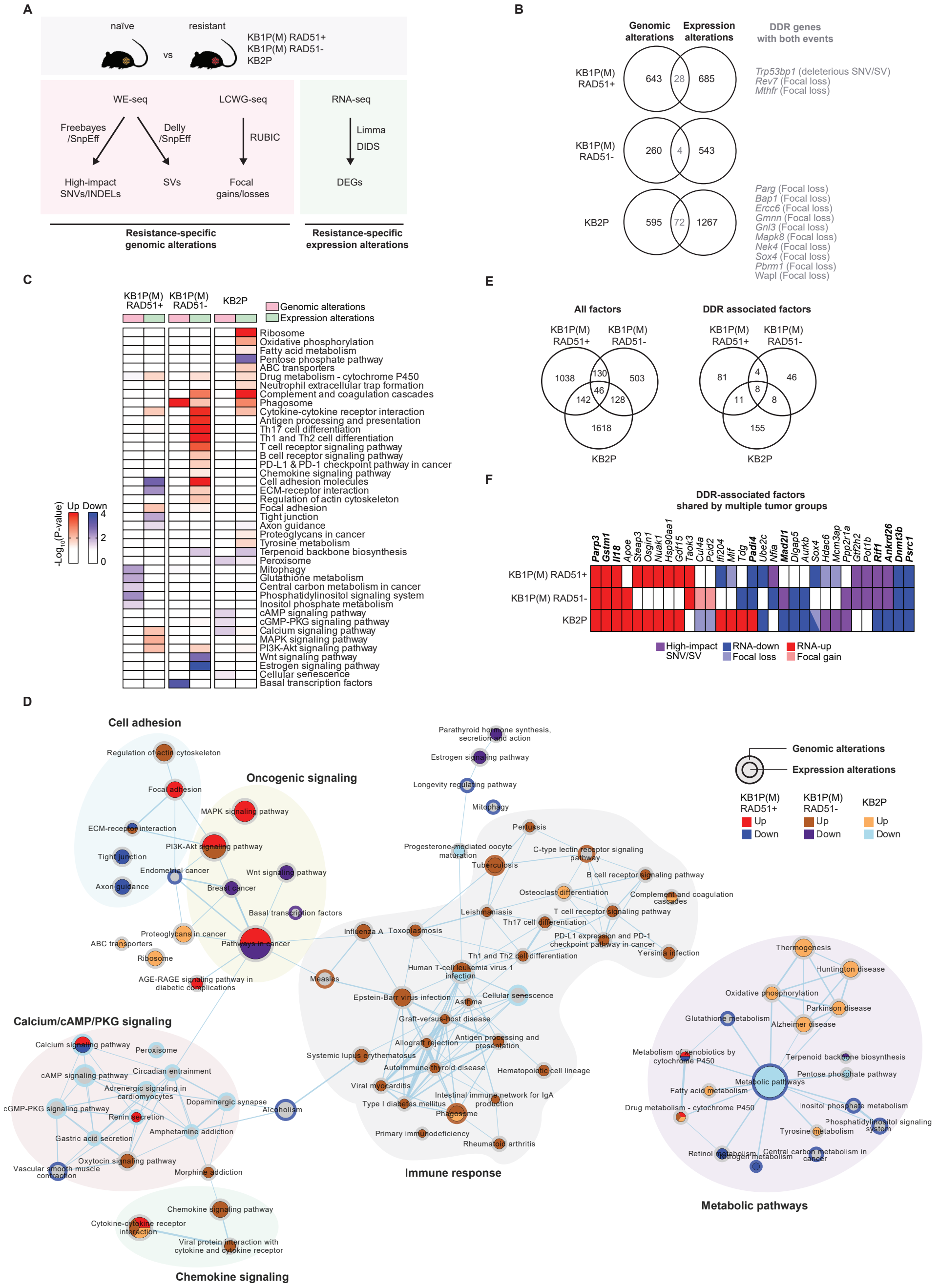

Figure 4 | Multi-omics analysis identifies potential PARPi-resistance factors/pathways. A | Schematic overview of the analysis to identify resistance-specific genomic and transcriptional alterations from WE-Seq, LCWG-Seq, and RNA-seq data. For each PARPi naïve and resistant RAD51-positive and RAD51-negative KB1P(M) and KB2P tumors, (1) deleterious SNVs, INDELs, SVs, and focal amplifications/deletions (resistance-specific genomic alterations) and (2) DEG sets identified by either limma or DIDS analysis (resistance-specific transcriptional alterations) were selected. DEG sets were extended to capture the genes with both homogeneous (by limma) and heterogenous behavior (by DIDS) between naïve and resistant tumors. **B |** Venn diagrams showing the overlaps between the genes having resistance-specific genomic alterations (SNVs, INDELs, SVs, and copy number focal gains and losses) and transcriptional alterations (DEGs) in each resistant tumor type. **C |** Heatmap of pathways significantly enriched by the genes with resistance-specific genomic and transcriptional alterations. Enrichment, $-\log_{10}$(P-value) computed by fisher exact test, by upregulated and downregulated genes are represented by red and green in the heatmap, respectively. **D |** Pathway enrichment map for genes with resistance-specific genomic and transcriptional alterations constructed by EnrichmentMap[63]. Node size represents size (number of genes) of gene sets (pathways) and edges represent mutual overlaps between the gene sets (minimum similarity score 0.3). Node and border represent enrichment by the genes with resistance-specific transcriptional and genomic alterations, respectively. **E |** Venn diagrams showing the overlaps of the genes having resistance-specific alterations with either genomic or transcriptional alterations across the three resistant tumor types. **F |** List of DDR-associated genes with resistance-specific alterations that were identified in multiple resistant tumor types.

DISCUSSION

In this study, we combined functional analysis of HR status with multi-omics analysis of a collection of matched PARPi-naïve and PARPi-resistant BRCA1-KO and BRCA2-KO mouse mammary tumors to classify the contribution of previously reported non-reversion resistance mechanisms in a preclinical "*in vivo* reality" of spontaneous acquired resistance. Overall, our analysis highlights the differences in resistance patterns between BRCA1- and BRCA2-deficient tumors and identifies HR restoration via loss of 53BP1 and restoration of PARP signaling via loss of PARG as the two dominant non-reversion resistance mechanisms in BRCA1- and BRCA2-deficient tumors, respectively. Additionally, our analysis generated a catalogue of candidate genes and pathways potentially involved in modulating PARPi response. Expanding the use of PARPi in the clinic should soon provide clinical specimens that will allow us to verify the relevance of our findings.

Functional differences between BRCA1 and BRCA2 impact PARPi resistance patterns

In our study we also used PARPi resistance as a tool to probe for different activities of BRCA1 and BRCA2 in DNA repair. BRCA1 and BRCA2 are often mentioned together, partly owing to their tumor suppressor activities and roles in HR repair. From a biological standpoint, however, BRCA1 and BRCA2 are not functionally redundant in HR. The epistatic relationship between BRCA1 and BRCA2 was first put forward in the context of embryonic lethality by Ludwig *et al.* almost 20 years ago[51]. Consistent with this relationship, previous work from our laboratory demonstrated that concomitant tissue-specific deletion of the *Brca1* and *Brca2* genes (KB1B2P) resulted in similar tumor development as single gene knockouts (KB1P and KB2P), indicating that BRCA1 and BRCA2 are epistatic in tumor suppression (Liu et al., unpublished data). Our present analysis of PARPi resistance mechanisms reveals a clear functional distinction between BRCA1 and BRCA2 in DNA repair. While HR-deficiency and PARPi sensitivity of BRCA1-KO tumors could be largely suppressed by inactivation of the 53BP1-RIF1-shieldin pathway, BRCA2-KO tumors completely failed to rescue HR activity, as measured by RAD51 foci formation, underlying the essential role of BRCA2 in RAD51 loading during the HR process. Moreover, we found that the levels of the RAD51-IRIF in the PARPi-resistant KB1P(M) tumors were significantly lower than in BRCA-proficient controls, indicating partial restoration of HR activity in these samples (**Supplementary Fig. 1C**). This is consistent with previous DR-GFP-based HR reporter assays we performed in *Tp53bp1*- or *Rev7*-depleted KB1P cells[23]. In addition, recent studies have suggested that whereas BRCA1 is dispensable for DNA end resection, its interaction with PALB2 and the resulting promotion of RAD51 loading cannot be fully compensated[52,53]. It is therefore conceivable that inactivation of the 53BP1-RIF1-shieldin pathway in BRCA1-KO tumors rescues the DNA end resection defect, but fails to fully restore HR repair due to lack of BRCA1 activity downstream of resection. Altogether, these data show that BRCA1 and BRCA2 are not epistatic in the repair of DSBs by HR and that these differences impact the resistance patterns in PARPi-treated tumors.

Resistance mechanisms in HR-restored BRCA1-KO tumors

Loss of 53BP1 was the most frequent alteration in RAD51-positive PARPi-resistant KB1P(M) tumors, whereas all other DSB end-protection factors seemed to be only sporadic. In line with this, mice bearing *Shld1/2*- or *Ctc1*-mutated KB1P tumors exhibit only partial response to olaparib in comparison with mice bearing unmodified KB1P tumors, whereas mice bearing *Trp53bp1*-mutated tumors did not respond to PARPi treatment, resulting in survival curves identical to vehicle-treated mice[17,54]. Moreover, loss of 53BP1 has also been observed in patient-derived tumor xenograft (PDX) models with acquired resistance to PARPi, and mutations in *TP53BP1* have been reported in tumor biopsies from patients with metastatic BRCA1-associated breast cancer receiving platinum chemotherapy or PARPi[19,55,56]. Altogether, our results indicate that BRCA1-independent HR restoration driven by inactivation of 53BP1 may be the most common mechanism of PARPi resistance in patients with *BRCA1*-mutated tumors that do not undergo BRCA1 reactivation, and that 53BP1 may be a potential biomarker of PARPi response in *BRCA1*-mutated tumors.

Resistance mechanisms in HR-deficient BRCA1-KO tumors

More than one-third of all PARPi-resistant KB1P(M) tumors were RAD51-negative, indicating that they hadn’t restored HR. Despite the fact that alterations in previously reported resistance factors were found sporadically in PARPi-resistant RAD51-negative KB1P(M) tumors, none of these factors were found significantly altered in any of the analyses carried out in this study. Moreover, alterations in these factors did not occur more frequently in PARPi-resistant RAD51-negative KB1P(M) tumors compared to PARPi-resistant RAD51-positive KB1P(M) or KB2P tumors. Nevertheless, gene set analysis of the DEGs identified in PARPi-resistant RAD51-negative KB1P(M) tumors yielded an enrichment in positive regulation of immune response which was in line with the increase in immune infiltration detected by IHC analysis. In line with this, organoids derived from one of the PARPi-resistant RAD51-negative KB1P(M) tumors (KB1PM7) failed to recapitulate PARPi resistance *in vitro* but upheld PARPi resistance *in vivo*, suggesting PARPi resistance in this tumor may be driven via cell-extrinsic processes that can only be recapitulated *in vivo*[57]. Moreover, these tumors preserve PARPi resistance following orthotopic transplantation of tumor fragments into syngeneic mice, indicating that the resistance phenotype is tumor-intrinsic.

Previous studies have reported that *BRCA1/2*-mutated tumors display increased immune infiltration upon treatment with PARPi, suggesting immune infiltration is required for PARPi antitumor efficacy[58]. Interestingly, among the different pathways upregulated in PARPi-resistant RAD51-negative KB1P(M) tumors, we identified an enrichment in factors associated with upregulation of PD-L1 and PD-1 checkpoint pathway, which is in line with the previously reported upregulation of PD-L1 expression by PARPi[59]. PARPi-resistant HR-deficient *BRCA1*-mutated tumors might therefore be treated with combinations of PARPi and immune-checkpoint inhibitors[59–61]. Altogether, these data highlight the role of the tumor microenvironment in the response to PARPi.

Resistance mechanisms in BRCA2-KO tumors

PARG loss was undoubtedly the most frequent alteration in PARPi-resistant KB2P tumors and occurred significantly more often in KB2P tumors than in the other tumor groups, even though a few resistant KB1P(M) tumors carried copy number loss and/or downregulation of *Parg*. The strong selection for PARG loss in KB2P tumors could result from of the impossibility of HR restoration in these tumors. Even so, PARG loss was not more frequent in PARPi-resistant HR-negative KB1P(M) tumors compared to HR-positive KB1P(M) tumors.

Perturbations that occurred more frequently in PARPi-resistant BRCA2-KO tumors than in BRCA1-KO tumors were alterations associated with loss of PARP trapping or rescue of PARP signaling (44% in KB2P versus 32% in KB1P(M); mostly involving *Parg*) and alterations associated with restoration of replication fork stability (56% in KB2P versus 35% in KB1P(M); mostly involving sporadic alterations). Unlike PARG, perturbations in PARP1 were anecdotal in both KB1P and KB2P tumors, suggesting PARP1 activity is critical for the viability of BRCA1/2-deficient cells.

Overall, our data show that PARPi resistance cannot be achieved via HR restoration in BRCA2-deficient tumors that cannot undergo BRCA2 reactivation. Moreover, loss of PARG is the single most recurrent driver of acquired resistance in BRCA2-KO tumors, yielding PARG as a potential predictive marker of PARPi response in patients with *BRCA2*-mutated tumors.

Limitations of this study

Our tumor collection recapitulates BRCA1/2 loss-driven tumor formation and acquired PARPi resistance but does not capture the full complexity of the human cancer (e.g., metastatic disease, heterogeneity, hypomorphic mutations). Moreover, human genes do not always have mouse orthologs or play exactly the same functions across the two species. For example, the previously reported PARPi resistance factor SLFN11[13] does not have a mouse ortholog and that is why it was not included in our analysis.

This study relies on the comparison with naïve tumors but does not include the comparison with responsive tumors (before developing resistance). Such tumor cohort would allow to identify gene/pathways altered during PARPi treatment before the tumors develop resistance. Additionally, the multi-omics analysis carried out in this study does not include methylome data and thus we might miss epigenetic mechanisms of PARPi resistance. Nevertheless, changes in DNA-methylation are predicted to affect transcriptional activity and should therefore be visible in the RNA-seq data.

In this study we carried out *in vitro* loss-of-function screens in two human cell lines to validate candidate drivers of *in vivo* PARPi resistance, however this approach failed to yield common hits other than the already-known factor *REV7*. A limitation of this approach is that loss-of-function screens, such as shRNA-based screens, can only functionally validate candidate loss-of-function factors, which represent 40% (356/891) of all candidate drivers. Additionally, PARPi resistance in tumors without alterations in known resistance genes could be driven by the additive effect of multiple alterations rather than a single event. Finally, resistance could be driven by genes that modulate the tumor microenvironment, which cannot be adequately modeled in *in vitro* screens.

ACKNOWLEDGMENTS

We thank the members of the Preclinical Intervention Unit of the Mouse Clinic for Cancer and Ageing (MCCA) at the NKI for their technical support with the animal studies. We also thank the following NKI core facilities for their excellent service: Animal Pathology facility, Digital Microscopy facility, Genomics Core facility and Animal facility. We would like to thank Piet Borst (NKI, Amsterdam) for scientific discussions. This work was funded by Oncode Institute, the Dutch Cancer Society (KWF 2011-5220 and 2014-6532), the Netherlands Organization for Scientific Research (VICI 91814643), the Netherlands Genomics Initiative (93512009), the Swiss National Science Foundation (310030_179360), the Swiss Cancer League (KLS-4282-08-2017), the Wilhelm-Sander Foundation (no. 2019.069.1) and the European Research Council (ERC-2019-AdG-883877, SyG-319661).

AUTHOR CONTRIBUTIONS

Conceptualization, J.B., M.P.D., E.G., S.R., J.J.; Methodology, J.B., M.P.D., E.G., F.R., S.R.P.; Investigation, J.B., M.P.D., E.G., F.R., A.A.D., W.S., I.v.d.H, L.B., T.S.K., B.M.; Software Analysis, J.B., E.G., F.R., B.v.d.B., J.R.d.R., R.d.B., R.L.B., C.L.; Original Draft, Review & Editing – J.B., M.P.D., E.G., L.F.A.W., S.R., J.J.; Supervision, M.v.d.V., C.R.J., L.F.A.W., S.R., J.J.; Funding Acquisition, S.R. and J.J.

METHODS

EXPERIMENTAL MODEL AND SUBJECT DETAILS

Cell Lines and cell culture

KB1P (KB1P-G3)[38] and KB2P (KB2P-3.4)[64] mouse tumor-derived cell lines were previously described and were grown in DMEM/F12 (Gibco) supplemented with 10% FBS and 50 units/ml penicillin-streptomycin (Gibco), containing 5 μg/ml Insulin (Sigma), 5 ng/ml cholera toxin (Sigma) and 5 ng/ml murine epidermal growth-factor (Sigma), under low oxygen conditions (3% O_2, 5% CO_2 at 37°C). RPE1-hTERT *BRCA1*$^{-/-}$*;TRP53*$^{-/-}$ human cell line has been described before [53] and was grown in DMEM+GlutaMAX (Gibco) supplemented with 10% FBS and 50 units/ml penicillin-streptomycin (Gibco), under low oxygen conditions (3% O_2, 5% CO_2 at 37°C) . SUM149PT (RRID:CVCL_3422) human cell line was grown in RPMI1640 (Gibco) medium supplied with 10% FBS and 50 units/ml penicillin-streptomycin (Gibco), under normal oxygen conditions (21% O2, 5% CO_2, 37°C).

Mice

All animal experiments were approved by the Animal Ethics Committee of The Netherlands Cancer Institute (Amsterdam, the Netherlands) and performed in accordance with the Dutch Act on Animal Experimentation (November 2014). Parental FVB (FVB/NRj) and 129/Ola animals were purchased from Janvier Labs and Harlan Olac, respectively, and crossed at the NKI Animal Facility.

METHOD DETAILS

In situ **RAD51-IRIF and 53BP1-IRIF assay**

Cryopreserved material of PARPi-naïve or -resistant KB1P, KB1PM and KB2P tumors (KB1P(M): 23 naïve, 47 resistant; KB2P: 19 naïve, 26 resistant) was thawed and orthotopically engrafted into the right mammary fat pad of 6 week-old wild-type syngeneic female mice (KB1P(M) – FVB; KB2P – FVB:129/Ola(F1)). Tumor volume was monitored starting from two weeks after transplantations and calculated using the following formula: 0.5 x length x width^2. When tumors reached approximately 500 mm^3 (100% relative tumor volume), they were locally irradiated using a CT-guided high precision cone beam micro-irradiator (X-RAD 225Cx) or left untreated (control). Two different factors were tested to optimize the assay: IR dosage (15 and 24 Gy) and post-irradiation incubation time (1-6 hr). We did not observe significant differences in RAD51 IRIF formation between the two IR dosages, and the highest accumulation of RAD51 foci was detected 2 hours after induction of DNA damage. Based on these results, we analyzed RAD51 IRIF in KB1P(M) and KB2P tumors 2 hr after irradiation with 15Gy. Post irradiation, tumors were isolated and part of the tissue was immediately fixed in 4% (w/v) solution of formaldehyde in PBS (remaining tissue was fresh frozen for the proteomic and phosphoproteomic analyses). 5 μm-thick FFPE (formalin-fixed paraffin embedded) tissue sections were then used for immunofluorescence. Following deparaffinization (70°C, 20 min), tissues were rehydrated and cooked in DAKO Target Retrieval Solution pH 9 (#S236784, DAKO) for 20 min in microwave at ~600W, to allow antigen retrieval. Next, tissue permeabilization was achieved by incubating samples in 0.2% (v/v) Triton X-100 in PBS for 20 min and followed by 1 hr DNAse (1,000 U/ml; #04536282001, Roche) treatment at 37°C. Blocking was done for 30 min in staining buffer (1% (w/v) BSA, 0.15% (w/v) glycine and 0.1% (v/v) Triton X-100 in PBS). Subsequent incubation with primary antibodies was carried out overnight at 4°C, and later with secondary antibodies for 1 hr at room temperature. The following antibodies (diluted in staining buffer) were used in this assay: rabbit polyclonal anti-RAD51 (kind gift from R. Kanaar, Erasmus MC, Rotterdam; 1:5,000), rabbit polyclonal anti-53BP1 (#ab21083, Abcam; 1:1,000), goat polyclonal anti-rabbit, Alexa Fluor® 658-conjugated (#A11011, Thermo Fisher Scientific; diluted 1:1,000). Samples were mounted with VECTASHIELD Hard Set Mounting Media with DAPI (#H-1500; Vector Laboratories). Images were taken with Leica SP5 (Leica Microsystems) confocal system equipped with a x100 objective and image stacks (~6 slices) were analyzed using an in-house developed ImageJ macro to automatically and objectively quantify IR-induced foci, as described before[23]. Briefly, nuclei were segmented by thresholding the (median-filtered) DAPI signal, followed by a watershed operation to separate touching nuclei. For each *z*-stack the maximum-intensity projection of the foci signal was background-subtracted using a difference of gaussians method. Next, for every nucleus, foci candidates were identified as locations where the resulting pixel values exceeded the background by a factor (typically 25x) times the median standard deviation of all nuclei in the image. Additional filters for discriminating for foci size, nucleus size (to eliminate stromal cells) and absolute brightness were applied. Results were validated by visual inspection. Visualization as well as quantification of foci was done in a blinded fashion. For each sample, five random areas (246 x 246 µm; on average 125 cells per area) were imaged and analyzed. Cell was considered positive if contained >5 nuclear foci. KP tumor was used as a positive control in this assay.

53BP1 IHC

All IHC stainings were performed on FFPE material. For 53BP1 IHC, tissue sections were boiled for 30 min in citrate buffer pH 6.0 (#CBB 999, Scytek Laboratories) to facilitate antigen retrieval. Next, the stainings were carried out by using 3% (v/v) H_2O_2 solution in methanol for blocking endogenous peroxidase activity (20 min) and 4% BSA plus 5% normal goat serum (NGS) in PBS as a blocking buffer (30 min). Primary antibodies were diluted in 1.25% NGS plus 1% BSA in PBS, and applied on the samples overnight, at 4°C. Incubation with secondary antibodies (diluted in 1.25% NGS/1% BSA in PBS; 30 min, room temperature) (#E0433, DakoCytomation) was followed by incubation with streptavidin conjugated to horseradish peroxidase (1:200; 1.25% NGS/1% BSA in PBS; 30 min) (#P0397, DakoCytomation). For visualization DAB (#D5905, Sigma), H_2O_2 (#A-31642, Sigma, 1:1,250) and hematoxylin counterstaining were applied. IHC stainings were evaluated and scored (0 – negative, 1 – low expression, 2 – high expression) by a pathologist who was blinded regarding the identity of the samples. Antibodies used in this protocol: rabbit polyclonal anti-53BP1 (#A300-272A, Bethyl Laboratories; 1:1,000), secondary donkey-anti-goat-Bio (#E0433, DakoCytomation; 1:200), secondary goat-anti-rabbit-Bio (#E0432, Dako Cytomation; 1:1,000).

Whole-exome sequencing (WE-seq)

Genomic DNA was isolated from fresh frozen tumor tissue using a standard Proteinase K and phenol:chloroform extraction and sheared to approximately 300 bp fragments using Covaris S2 sonicator. Next, 500-1000 ng of sheared DNA was used as a template for a 6-cycle PCR to construct a fragmented library using the KAPA HTP Library Preparation Kit (Roche). Exome enrichment was performed using SeqCap EZ Enrichment Kit (Roche) according to the manufacturer's protocol (SeqCap EZ Library SR User's Guide, v5.3). Samples were sequenced on an Illumina HiSeq2500 (Illumina). Adapters in the resulting reads were trimmed using Cutadapt[65] (version 1.12) and the trimmed reads were aligned to the GRCm38 reference genome using BWA (version 0.7.15)[66]. The resulting alignments were sorted and marked for duplicates with Picard tools (version 2.5.0). Freebayes variant caller was used to identify SNVs and Indels for each sample with the mode of pooled-continuous (min-alternate-fraction = 0.1, min-alternate-count = 3, and min-coverage = 10)[67] and resulting variants were annotated by SnpEff[68]. SNVs and Indels identified in FVB/NJ mice were obtained from Sanger Mouse Genome Project[69] and used to discard germline variants in our tumor samples. SNVs and Indels that were only identified in resistant tumors and predicted to be high-impact mutations by SnpEff were considered resistant tumor-specific alterations with functional effects and were used for downstream analysis. Structural variants were identified by delly (version 0.9.1) for each pair of resistant and matched naïve tumors and resulting variants were annotated by SnpEff. High-impact SVs predicted by SnpEff were used for downstream analysis.

Low-coverage whole-genome sequencing (LCWG-seq)

LCWG-seq data was generated as described before [9]. Briefly, genomic DNA was isolated from fresh-frozen tumor material using standard phenol:chloroform extraction. LCWG-seq was performed using double stranded DNA (dsDNA) and quantified with the Qubit® dsDNA HS Assay Kit (Invitrogen, #Q32851). Library preparation was performed with 1 μg of DNA and KAPA HTP Library Preparation Kit (KAPA Biosystems, #KK8234). Resulting reads (50 base single-end reads) were trimmed, sorted and marked for duplicates using the same pipeline as for the WES. The resulting alignments were analyzed to generate segmented profile differences between matched (naïve/resistant) samples derived from the same tumor donor using the QDNAseq and QDNAseq.mm10 R packages (bin size = 50K)[70]. To identify regions with recurrent copy number difference (naïve vs resistant), we iteratively ran RUBIC with default cutoff for calling amplifications and deletions (focal threshold = 1e+08, min probes = 4, FDR < 0.25, amp.level and del.level = 0.1)[47].

RNA sequencing (RNA-seq)

RNA-seq data was generated as described before[9]. Briefly, fresh frozen tumor tissue were placed in 1 ml of TRIsure reagent (#BIO-38032, Bioline) and tissue lysis was achieved by high-speed shaking with stainless steel beads for 10 min, 50 Hz at room temperature (TissueLyser LT, Qiagen). Homogenized tissue lysates were further processed according to the TRIsure manufacturer's protocol. Strand-specific libraries were generated using the TruSeq Stranded mRNA sample preparation kit (Illumina Inc., San Diego, RS-122-2101/2) according to the manufacturer's instructions. The resulting reads (50 base single-end reads) were trimmed using Cutadapt[65] and aligned to the GRCm38 reference genome using STAR (version 2.5.2b)[71]. To identify differentially expressed (DE) genes, gene expression counts were first generated by featureCounts using gene definitions from Ensembl GRCm38 (version 76)[72]. Genes with counts per million (CPM) larger than one in at least 10% of samples were used for further analysis. Trimmed mean of M-value (TMM) normalization was applied to the data using edgeR[73] and Limma-voom was used to correct for the donor effect and identify the differentially expressed genes between naïve vs resistant tumors ($FDR < 0.25$ for KB1P and $FDR<0.05$ for KB2P, Log2 fold change>0.5)[74]. Because of the intratumoral heterogeneity, we additionally applied DIDS (Detection of Imbalanced Differential Signal) for the detection of subgroup markers in resistant populations ($P < 0.05$)[44].

Selection of previously reported PARPi resistance factors

The list of resistance-associated factors was generated based on previous reports[7]. We excluded *SLFN11*[13] which does not have a mouse ortholog and *Shld3* and *Radx* which were not expressed in our mouse cohort. In total, 25 genes were analyzed in our omics datasets **(Supplementary table 1)**.

Selection of DNA damage response (DDR)-related genes

The DDR gene set was obtained from the previous study that was generated based by merging the gene lists from the previous papers and the NCBI search by terms of "DNA repair", "DNA damage response", "DNA replication", and "telomere-associated genes"[9].

Gene set over-representation analysis

Gene set over-representation analysis was performed by DAVID[75] for genes with significant upregulation and downregulation (RNA-seq) and focal gains and losses (CNV-seq) in resistant tumors compared to naïve tumors. The significant gene sets were identified as the ones with $P<0.05$.

Driver gene analysis

For genes with resistant tumor-specific mutations and copy number variations as mentioned above, DriverNet was used to infer potential driver genes by assessing the impact of alterations on the expression network. Protein-protein interactome (PPI) to construct expression network was obtained by orthologue mapping of human PPI merged from multiple PPI databases[76–80]. The genes with more than 1.5-fold changes in expression were defined as genes showing outlying expression and used to assess the impact of mutations in the expression network. P-value was computed by gene-based randomization of 1000 times and genes with P-value <0.05 were selected as potential drivers.

Mass spectrometry (MS)-based proteomics

For the proteomic and phosphoproteomic analyses of KB1P(M) tumors, we used previously published proteomics dataset generated by MS (PRIDE accession code: PXD032007)[81]. For phosphoproteomic analysis, for phosphoproteomic analysis, MaxQuant phosphosite quantification data (Phospho (STY)Sites.txt) was log2-transformed, normalized on the median intensity of all identified phosphosites and replicates averaged favoring data presence. For global protein expression analysis, MaxQuant LFQ Intensity[82] was log2-transformed and replicates were averaged. limma[48] was used for differential expression analysis.

Shld2 gene-editing

For CRISPR/Cas9-mediated genome editing of *Shld2,* sgRNA sequences (sgRNA#1: 5'-atcagtcagatccctgcgtt-3'; sgRNA#2: 5'-aacctgagtgatatgactag-3') were cloned into a modified version of the lentiCRISPR v2 backbone (RRID: Addgene_52961) in which a puromycin resistance ORF was cloned under the hPGK promoter, or into the pX330.puro backbone (Addgene #110403). Cloning of sgRNAs into the lentiCRISPR v2 backbone was carried out by melting the custom DNA oligos (Microsynth) at 95°C for 5 min, followed by annealing at RT for 2h and subsequently ligation with T4 ligase (NEB) into the BsmBI-digested (Fermantas) backbone. Cloning of sgRNAs into the pX330.puro backbone was performed similarly by ligating the previously annealed oligos into the BbsI-HF-digested backbone with T4 ligase (NEB). KB2P tumor-derived cells were transduced with the cloned lentiCRISPR v2 constructs and KB1P cells were transfected with the generated pX330.puro plasmids using a transfection reagent (TransIT-LT1 from Mirus) following the manufacturer's protocol. All constructs' sequences were verified by Sanger sequencing.

Lentiviral Transductions

Lentiviral stocks, pseudotyped with the VSV-G envelope, were generated by transient transfection of HEK293FT cells, as described before[83]. Production of integration-deficient lentivirus (IDLV) stocks was carried out in a similar fashion, with the exception that the packaging plasmid contains a point mutation in the integrase gene (psPAX2, gift from Bastian Evers). Lentiviral titers were determined using the qPCR Lentivirus Titration Kit (Applied Biological Materials), following the manufacturer's instructions. Cells were incubated with lentiviral supernatants overnight in the presence of polybrene (8 μg/ml). Antibiotic selection was initiated 24h after transduction and was carried out for 3 consecutive days.

Long-Term Clonogenic Assays

Long-term clonogenic assays were always performed in 6-well plates. KB1P and KB2P tumor-derived cells were seeded at low density to avoid contact inhibition between the clones (4,000 and 3,000 cells/well, respectively). Control untreated plates were fixed with 4% formaldehyde between days 7 and 8 and treated plates between days 8 and 14. For the quantification, cells were stained with 0.1% crystal violet and analyzed in an automated manner using the ImageJ ColonyArea plugin previously described[84].

Functional Genetic Enrichment Screens

We have generated a focused shRNA library targeting the human candidate genes plus non-essential genes as controls, resulting in a total of 1025 genes. We selected 5 hairpins per gene, less when 5 weren't available, resulting in 5062 lentiviral hairpins (pLKO.1) from the Sigma Mission library (TRC 1.0 and 2.0) **(Supplementary table 5)**. This library was then used to generate pools of lentiviral shRNAs which were then transduced in RPE1-hTERT *BRCA1*$^{-/-}$;*TRP53*$^{-/-}$ and SUM149PT human cells, as described in the section *Lentiviral Transductions*. Lentiviral transductions were carried out using a multiplicity of transduction (MOI) of 0.3, in order to ensure that each cell only gets incorporated with one only sgRNA. After transduction, the cells stably expressing integrated shRNA were selected with puromycin. After selection, cells were collected (T0) or seeded in the presence of PARPi (SUM149PT:100.000 cells p/ 15 cm plate, 10nM olaparib; RPE1-hTERT *BRCA1*$^{-/-}$;*TRP53*$^{-/-}$: 50.000 cells p/ 15 cm plate, 50nM olaparib). The total number of cells used in a single screen was calculated as following: library complexity x coverage (1000x). Triplicates were carried out for both cell lines. Cells were kept in culture for 3 weeks and medium was refreshed every 5 days. In the end of the screen, or at T0, cells were pooled and genomic DNA was extracted (QIAmp DNA Mini Kit, Qiagen). shRNA sequences were retrieved by a two-step PCR amplification, as described before[23]. To maintain screening coverage, the amount of genomic DNA used as an input for the first PCR reaction was taken into account (6 µg of genomic DNA per 10^6 genomes, 1 µg/PCR reaction). Resulting PCR products were purified using MiniElute PCR Purification Kit (Qiagen) and submitted for Illumina sequencing. Sequence alignment and dropout analysis was carried out using the algorithm MaGECK (Li et al., 2014).

DATA AND SOFTWARE AVAILABILITY

Sequencing of all functional genetic screens was performed at the Netherlands Cancer Institute and results will be made available upon request. The accession number for the raw data of WE-seq, LCWG-seq and RNA-seq reported in this chapter is European Nucleotide Archive (ENA): PRJEB25803.

REFERENCES

1. Farmer, H. *et al.* Targeting the DNA repair defect in BRCA mutant cells as a therapeutic strategy. *Nature* **434**, 917–21 (2005).
2. Bryant, H. E. *et al.* Specific killing of BRCA2-deficient tumours with inhibitors of poly(ADP-ribose) polymerase. *Nature* **434**, 913–917 (2005).
3. Scully, R., Panday, A., Elango, R. & Willis, N. A. DNA double-strand break repair-pathway choice in somatic mammalian cells. *Nat. Rev. Mol. Cell Biol.* **20**, 698–714 (2019).
4. Ray Chaudhuri, A. & Nussenzweig, A. The multifaceted roles of PARP1 in DNA repair and chromatin remodelling. (2017). doi:10.1038/nrm.2017.53
5. Murai, J. *et al.* Trapping of PARP1 and PARP2 by clinical PARP inhibitors. *Cancer Res.* **72**, 5588–5599 (2012).
6. Lupo, B. & Trusolino, L. Inhibition of poly(ADP-ribosyl)ation in cancer: Old and new paradigms revisited. *Biochimica et Biophysica Acta - Reviews on Cancer* **1846**, 201–215 (2014).
7. Paes Dias, M., Moser, S. C., Ganesan, S. & Jonkers, J. Understanding and overcoming resistance to PARP inhibitors in cancer therapy. *Nature Reviews Clinical Oncology* 1–19 (2021).
8. Rottenberg, S. *et al.* Selective induction of chemotherapy resistance of mammary tumors in a conditional mouse model for hereditary breast cancer. *Proc. Natl. Acad. Sci. U. S. A.* **104**, 12117–12122 (2007).
9. Gogola, E. *et al.* Selective Loss of PARG Restores PARylation and Counteracts PARP Inhibitor-Mediated Synthetic Lethality. *Cancer Cell* **33**, 1078-1093.e12 (2018).
10. Pettitt, S. J. *et al.* A genetic screen using the PiggyBac transposon in haploid cells identifies Parp1 as a mediator of olaparib toxicity. *PLoS One* **8**, e61520 (2013).
11. Pettitt, S. J. *et al.* Genome-wide and high-density CRISPR-Cas9 screens identify point mutations in PARP1 causing PARP inhibitor resistance. *Nat. Commun.* **9**, 1849 (2018).
12. Murai, J. *et al.* SLFN11 Blocks Stressed Replication Forks Independently of ATR. *Mol. Cell* **69**, 371-384.e6 (2018).
13. Murai, J. *et al.* Resistance to PARP inhibitors by SLFN11 inactivation can be overcome by ATR inhibition. *Oncotarget* **7**, 76534–76550 (2016).
14. Cantor, S. B. & Calvo, J. A. Fork Protection and Therapy Resistance in Hereditary Breast Cancer. (2017).
15. Bunting, S. F. *et al.* 53BP1 Inhibits Homologous Recombination in Brca1-Deficient Cells by Blocking Resection of DNA Breaks. *Cell* **141**, 243–254 (2010).
16. Bouwman, P. *et al.* 53BP1 loss rescues BRCA1 deficiency and is associated with triple-negative and BRCA-mutated breast cancers. *Nat. Struct. Mol. Biol.* **17**, 688–695 (2010).
17. Noordermeer, S. M. *et al.* The shieldin complex mediates 53BP1-dependent DNA repair. *Nature* **560**, 117–121 (2018).
18. Gupta, R. *et al.* DNA Repair Network Analysis Reveals Shieldin as a Key Regulator of NHEJ and PARP Inhibitor Sensitivity. *Cell* **173**, 972-988.e23 (2018).
19. Dev, H. *et al.* Shieldin complex promotes DNA end-joining and counters homologous recombination in BRCA1-null cells. *Nat. Cell Biol.* **20**, 954–965 (2018).
20. Findlay, S. *et al.* SHLD 2/ FAM 35A co-operates with REV 7 to coordinate DNA double-strand break repair pathway choice. *EMBO J.* **37**, (2018).
21. Gao, S. *et al.* An OB-fold complex controls the repair pathways for DNA double-strand breaks. *Nat. Commun.* **9**, 1–10 (2018).
22. Tomida, J. *et al.* FAM 35A associates with REV 7 and modulates DNA damage responses of normal and BRCA 1-defective cells . *EMBO J.* **37**, e99543 (2018).
23. Xu, G. *et al.* REV7 counteracts DNA double-strand break resection and affects PARP inhibition. *Nature* **521**, 541–544 (2015).
24. Boersma, V. *et al.* MAD2L2 controls DNA repair at telomeres and DNA breaks by inhibiting 5' end resection. *Nature* **521**, 537–40 (2015).
25. Chapman, J. R. *et al.* RIF1 Is Essential for 53BP1-Dependent Nonhomologous End Joining and Suppression of DNA Double-Strand Break Resection. *Mol. Cell* **49**, 858–871 (2013).
26. Feng, L. *et al.* Cell cycle-dependent inhibition of 53BP1 signaling by BRCA1. *Cell Discov.* **1**, 15019 (2015).
27. Di Virgilio, M. *et al.* Rif1 prevents resection of DNA breaks and promotes immunoglobulin class switching. *Science (80-.).* **339**, 711–715 (2013).
28. Zimmermann, M., Lottersberger, F., Buonomo, S. B., Sfeir, A. & de Lange, T. 53BP1 Regulates DSB Repair Using Rif1 to Control 5' End Resection. *Science (80-.).* **339**, 700–704 (2013).
29. Escribano-Díaz, C. *et al.* A cell cycle-dependent regulatory circuit composed of 53BP1-RIF1 and BRCA1-CtIP controls DNA repair pathway choice. *Mol. Cell* **49**, 872–83 (2013).
30. Ghezraoui, H. *et al.* 53BP1 cooperation with the REV7–shieldin complex underpins DNA structure-specific NHEJ. *Nature* **560**, 122–127 (2018).
31. Ganesan, S. Tumor Suppressor Tolerance: Reversion Mutations in BRCA1 and BRCA2 and Resistance to PARP

Inhibitors and Platinum. *JCO Precis. Oncol.* 1–4 (2018).

32. Barber, L. J. *et al.* Secondary mutations in BRCA2 associated with clinical resistance to a PARP inhibitor. *J. Pathol.* **229**, 422–9 (2013).
33. Weigelt, B. *et al.* Diverse BRCA1 and BRCA2 Reversion Mutations in Circulating Cell-Free DNA of Therapy-Resistant Breast or Ovarian Cancer. *Clin. Cancer Res.* **23**, 6708–6720 (2017).
34. Domchek, S. M. Reversion Mutations with Clinical Use of PARP Inhibitors: Many Genes, Many Versions. *Cancer Discov.* **7**, 937–939 (2017).
35. Norquist, B. *et al.* Secondary somatic mutations restoring BRCA1/2 predict chemotherapy resistance in hereditary ovarian carcinomas. *J. Clin. Oncol.* **29**, 3008–3015 (2011).
36. Ang, J. E. *et al.* Efficacy of chemotherapy in BRCA1/2 mutation carrier ovarian cancer in the setting of PARP inhibitor resistance: a multi-institutional study. *Clin. Cancer Res.* **19**, 5485–93 (2013).
37. Litton, J. K. *et al.* Neoadjuvant Talazoparib for Patients With Operable Breast Cancer With a Germline BRCA Pathogenic Variant. *J. Clin. Oncol.* **38**, 388–394 (2020).
38. Jaspers, J. E. *et al.* Loss of 53BP1 causes PARP inhibitor resistance in BRCA1-mutated mouse mammary tumors. *Cancer Discov.* **3**, 68–81 (2013).
39. Jonkers, J. *et al.* Synergistic tumor suppressor activity of BRCA2 and p53 in a conditional mouse model for breast cancer. *Nat. Genet.* **29**, 418–425 (2001).
40. Liu, X. *et al.* Somatic loss of BRCA1 and p53 in mice induces mammary tumors with features of human BRCA1-mutated basal-like breast cancer. *Proc. Natl. Acad. Sci.* **104**, 12111–12116 (2007).
41. Ray Chaudhuri, A. *et al.* Replication fork stability confers chemoresistance in BRCA-deficient cells. *Nature* **535**, 382–387 (2016).
42. Oplustil O'Connor, L. *et al.* The PARP Inhibitor AZD2461 Provides Insights into the Role of PARP3 Inhibition for Both Synthetic Lethality and Tolerability with Chemotherapy in Preclinical Models. *Cancer Res.* **76**, 6084–6094 (2016).
43. Godin, S. K., Sullivan, M. R. & Bernstein, K. A. Novel insights into RAD51 activity and regulation during homologous recombination and DNA replication. *Biochem. Cell Biol.* **94**, 407–418 (2016).
44. de Ronde, J. J., Rigaill, G., Rottenberg, S., Rodenhuis, S. & Wessels, L. F. A. Identifying subgroup markers in heterogeneous populations. *Nucleic Acids Res.* **41**, e200–e200 (2013).
45. Kas, S. M. *et al.* Transcriptomics and Transposon Mutagenesis Identify Multiple Mechanisms of Resistance to the FGFR Inhibitor AZD4547. *Cancer Res.* **78**, 5668–5679 (2018).
46. Rondinelli, B. *et al.* EZH2 promotes degradation of stalled replication forks by recruiting MUS81 through histone H3 trimethylation. *Nat. Cell Biol.* **19**, 1371–1378 (2017).
47. van Dyk, E., Hoogstraat, M., Ten Hoeve, J., Reinders, M. J. T. & Wessels, L. F. A. RUBIC identifies driver genes by detecting recurrent DNA copy number breaks. *Nat. Commun.* **7**, 12159 (2016).
48. Ritchie, M. E. *et al.* limma powers differential expression analyses for RNA-sequencing and microarray studies. *Nucleic Acids Res.* **43**, e47–e47 (2015).
49. Bhattacharya, A. *et al.* Transcriptional effects of copy number alterations in a large set of human cancers. *Nat. Commun.* **11**, 1–12 (2020).
50. Bashashati, A. *et al.* DriverNet: uncovering the impact of somatic driver mutations on transcriptional networks in cancer. *Genome Biol.* **13**, R124–R124 (2012).
51. Ludwig, T., Chapman, D. L., Papaioannou, V. E. & Efstratiadis, A. Targeted mutations of breast cancer susceptibility gene homologs in mice: lethal phenotypes of Brca1, Brca2, Brca1/Brca2, Brca1/p53, and Brca2/p53 nullizygous embryos. *Genes Dev.* **11**, 1226–1241 (1997).
52. Nacson, J. *et al.* BRCA1 Mutation-Specific Responses to 53BP1 Loss-Induced Homologous Recombination and PARP Inhibitor Resistance. *Cell Rep.* **24**, 3513-3527.e7 (2018).
53. Belotserkovskaya, R. *et al.* PALB2 chromatin recruitment restores homologous recombination in BRCA1-deficient cells depleted of 53BP1. *Nat. Commun.* **11**, 1–11 (2020).
54. Barazas, M. *et al.* The CST Complex Mediates End Protection at Double-Strand Breaks and Promotes PARP Inhibitor Sensitivity in BRCA1-Deficient Cells. *Cell Rep.* **23**, 2107–2118 (2018).
55. Cruz, C. *et al.* RAD51 foci as a functional biomarker of homologous recombination repair and PARP inhibitor resistance in germline BRCA-mutated breast cancer. *Ann. Oncol.* **29**, 1203–1210 (2018).
56. Waks, A. G. *et al.* Reversion and non-reversion mechanisms of resistance to PARP inhibitor or platinum chemotherapy in BRCA1/2-mutant metastatic breast cancer. *Ann. Oncol.* **31**, 590–598 (2020).
57. Duarte, A. A. *et al.* BRCA-deficient mouse mammary tumor organoids to study cancer-drug resistance. *Nat. Methods* **15**, 134–140 (2018).
58. Pantelidou, C. *et al.* PARP Inhibitor Efficacy Depends on CD8 + T-cell Recruitment via Intratumoral STING Pathway Activation in BRCA-Deficient Models of Triple-Negative Breast Cancer. *Cancer Discov.* **9**, 722–737 (2019).
59. Jiao, S. *et al.* PARP Inhibitor Upregulates PD-L1 Expression and Enhances Cancer-Associated Immunosuppression. *Clin. Cancer Res.* **23**, 3711–3720 (2017).
60. Ding, L. *et al.* PARP Inhibition Elicits STING-Dependent Antitumor Immunity in Brca1-Deficient Ovarian Cancer.

Cell Rep. **25**, 2972-2980.e5 (2018).

61. Shen, J. *et al.* PARPi Triggers the STING-Dependent Immune Response and Enhances the Therapeutic Efficacy of Immune Checkpoint Blockade Independent of BRCAness. *Cancer Res.* **79**, 311–319 (2019).
62. Szklarczyk, D. *et al.* The STRING database in 2021: customizable protein-protein networks, and functional characterization of user-uploaded gene/measurement sets. *Nucleic Acids Res.* **49**, D605–D612 (2021).
63. Merico, D., Isserlin, R., Stueker, O., Emili, A. & Bader, G. D. Enrichment Map: A Network-Based Method for Gene-Set Enrichment Visualization and Interpretation. *PLoS One* **5**, e13984 (2010).
64. Evers, B. *et al.* Selective Inhibition of BRCA2-Deficient Mammary Tumor Cell Growth by AZD2281 and Cisplatin. *Clin. Cancer Res.* **14**, 3916–3925 (2008).
65. Martin, M. Cutadapt removes adapter sequences from high-throughput sequencing reads. *EMBnet.journal* **17**, 10 (2011).
66. Li, H. Aligning sequence reads, clone sequences and assembly contigs with BWA-MEM. (2013).
67. Garrison, E. & Marth, G. Haplotype-based variant detection from short-read sequencing. (2012).
68. Cingolani, P. *et al.* A program for annotating and predicting the effects of single nucleotide polymorphisms, SnpEff: SNPs in the genome of Drosophila melanogaster strain w1118; iso-2; iso-3. *Fly (Austin).* **6**, 80–92 (2012).
69. Keane, T. M. *et al.* Mouse genomic variation and its effect on phenotypes and gene regulation. *Nat. 2011 4777364* **477**, 289–294 (2011).
70. Scheinin, I. *et al.* DNA copy number analysis of fresh and formalin-fixed specimens by shallow whole-genome sequencing with identification and exclusion of problematic regions in the genome assembly. *Genome Res.* **24**, 2022–2032 (2014).
71. Dobin, A. *et al.* STAR: ultrafast universal RNA-seq aligner. *Bioinformatics* **29**, 15–21 (2013).
72. Liao, Y., Smyth, G. K. & Shi, W. featureCounts: an efficient general purpose program for assigning sequence reads to genomic features. *Bioinformatics* **30**, 923–930 (2013).
73. Robinson, M. D., McCarthy, D. J. & Smyth, G. K. edgeR: a Bioconductor package for differential expression analysis of digital gene expression data. *Bioinformatics* **26**, 139–140 (2010).
74. Law, C. W., Chen, Y., Shi, W. & Smyth, G. K. voom: Precision weights unlock linear model analysis tools for RNA-seq read counts. *Genome Biol.* **15**, R29–R29 (2014).
75. Prakash, R., Zhang, Y., Feng, W. & Jasin, M. Homologous recombination and human health: The roles of BRCA1, BRCA2, and associated proteins. *Cold Spring Harb. Perspect. Biol.* **7**, (2015).
76. Stark, C. *et al.* BioGRID: a general repository for interaction datasets. *Nucleic Acids Res.* **34**, (2006).
77. Xenarios, I. *et al.* DIP: the Database of Interacting Proteins. *Nucleic Acids Res.* **28**, 289 (2000).
78. Goel, R., Harsha, H. C., Pandey, A. & Keshava Prasad, T. S. Human Protein Reference Database and Human Proteinpedia as Resources for Phosphoproteome Analysis. doi:10.1039/c1mb05340j
79. Hermjakob, H. *et al.* IntAct: an open source molecular interaction database. *Nucleic Acids Res.* **32**, D452 (2004).
80. Kotlyar, M., Pastrello, C., Sheahan, N. & Jurisica, I. Integrated interactions database: tissue-specific view of the human and model organism interactomes. *Nucleic Acids Res.* **44**, D536–D541 (2016).
81. Zingg, D. *et al.* Truncated FGFR2 is a clinically actionable oncogene in multiple cancers. *Nat. 2022* 1–9 (2022).
82. Cox, J. *et al.* Accurate proteome-wide label-free quantification by delayed normalization and maximal peptide ratio extraction, termed MaxLFQ. *Mol. Cell. Proteomics* **13**, 2513–2526 (2014).
83. Follenzi, A., Ailles, L. E., Bakovic, S., Geuna, M. & Naldini, L. Gene transfer by lentiviral vectors is limited by nuclear translocation and rescued by HIV-1 pol sequences. *Nat. Genet.* **25**, 217–222 (2000).
84. Guzmán, C., Bagga, M., Kaur, A., Westermarck, J. & Abankwa, D. ColonyArea: an ImageJ plugin to automatically quantify colony formation in clonogenic assays. *PLoS One* **9**, (2014).

SUPPLEMENTARY FILES

Supplementary Tables 1-5 are available in the online version of the paper.

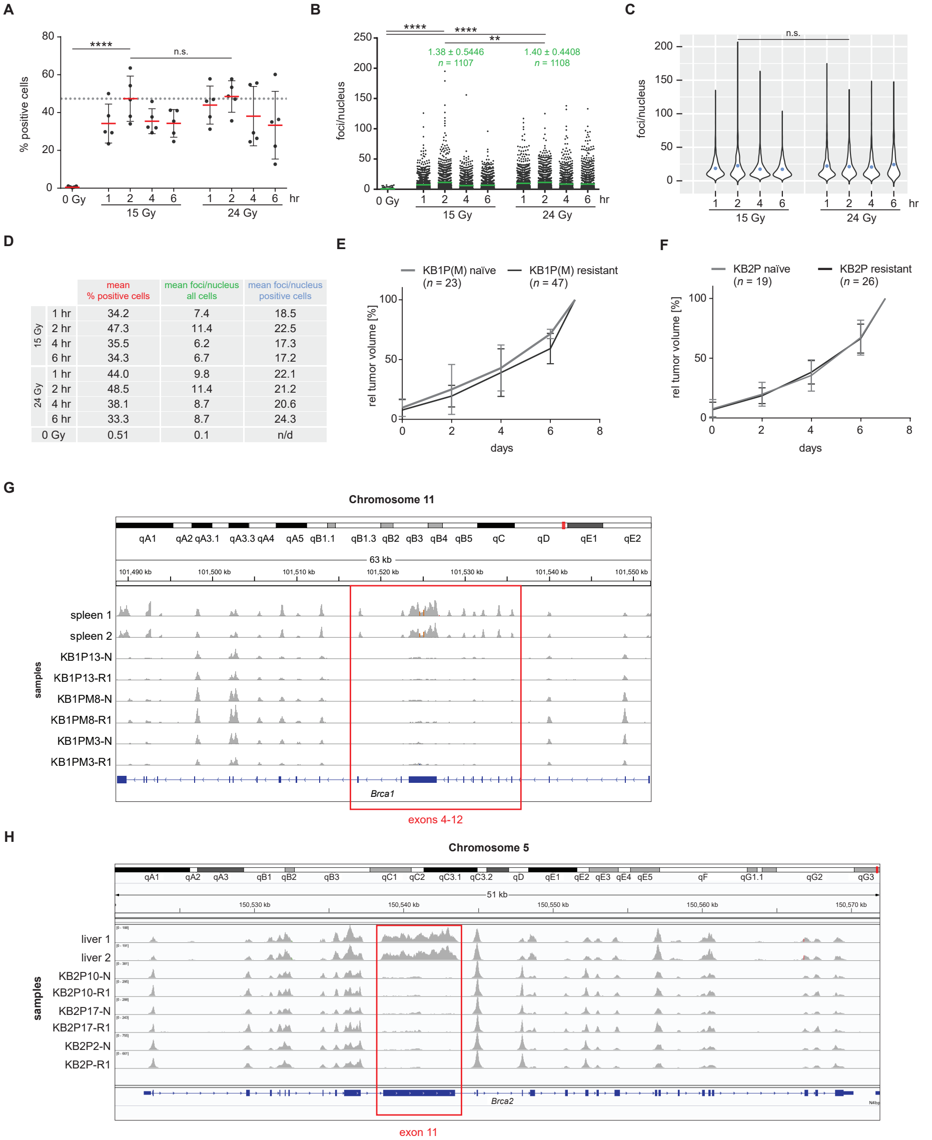

		mean % positive cells	mean foci/nucleus all cells	mean foci/nucleus positive cells
15 Gy	1 hr	34.2	7.4	18.5
	2 hr	47.3	11.4	22.5
	4 hr	35.5	6.2	17.3
	6 hr	34.3	6.7	17.2
24 Gy	1 hr	44.0	9.8	22.1
	2 hr	48.5	11.4	21.2
	4 hr	38.1	8.7	20.6
	6 hr	33.3	8.7	24.3
0 Gy		0.51	0.1	n/d

Supplementary figure 1 | Optimization of the RAD51 IRIF formation assay. Related to figure 1. A | Percentage of RAD51 positive cells (>5 foci/nucleus) per tumor area (single data point) in a KP tumor irradiated with 0, 15 or 24 Gy, 1-6 hr post-irradiation; ****p<0.0001, n.s. not significant (two-tailed Mann-Whitney U test); data shown as mean (red line) ± SD of a replicate, the experiment was repeated twice; grey dotted line indicates the mean value of a sample irradiated with 15 Gy and incubated for 2 hr. **B |** Number of foci per nucleus (single data point) quantified for the total tumor cell population of a KP described in (A); mean values are represented by green lines; **p<0.01, statistical analysis as in (A). **C |** Number of foci per nucleus quantified for positive cell population (>5 foci/nucleus) of a KP tumor described in (A), and represented as violin plots showing the density (width = frequency) of the data; mean values are represented by blue dots; statistical analysis as in (A). **D |** Summary of analyses represented in (A-C). **E-F |** Growth curves of KB1P(M) (E) and KB2P (F) tumors, samples were irradiated at day 7. **G-H |** Visualization of exome sequencing reads for the *Brca1* (G) and *Brca2* (H) genes in KB1P(M) and KB2P tumor samples, respectively; and normal tissues (spleen 1/2 and liver 1/2; controls), showing that deletions of specific exons (marked in red; *Brca1* – exons 4-12 (GRCm38, previously referred to as exons 5-13[40], *Brca2* – exon 11) are preserved in PARPi-naïve and PARPi-resistant tumor samples; data representative for the whole KB1P(M) and KB2P tumor panels.

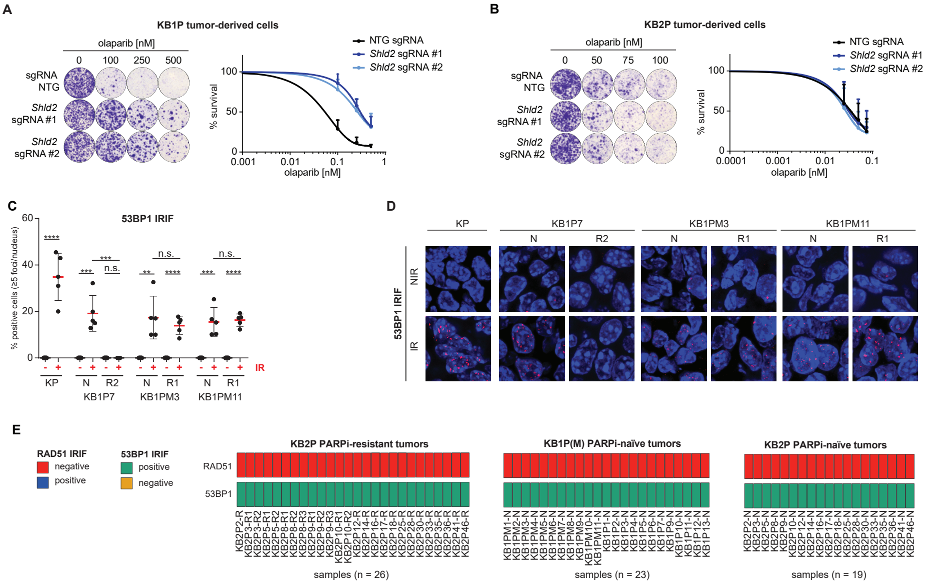

Supplementary figure 2 | *Trp53bp1* gene expression correlates with 53BP1 IRIF. Related to figure 2. **A-B |** Representative images (left) and quantification (right) of clonogenic assays in the presence of olaparib in KB1P (A) and KB2P (B) tumor-derived cells modified by CRISPR-Cas9 with the indicated sgRNAs. Control untreated plates were harvested on day 7/8 and treated plates on day 14. Statistical analysis was performed using 2-way ANOVA followed by Dunnett's test. *p < 0.05, **p < 0.01, ***p < 0.001. **C-D |** Representative images (A) and quantification (B) of 53BP1 IRIFs for the different matched KB1P(M) tumor pairs; IR – irradiated, NIR – non irradiated; scale bar, 100 µm; data in (B) represented as percentage of positive cells (≥5 foci/nucleus) per imaged area (single data point, typically 100-200 cells/area); ****p<0.0001, ***p<0.001, **p<0.01, n.s. not significant (two-tailed Mann-Whitney U test). **E |** Outcome of the RAD51 and 53BP1 IRIF assays for PARPi-resistant KB2P tumors and for PARPi-naïve KB1P(M) and KB2P tumors; N – naïve; R – resistant.

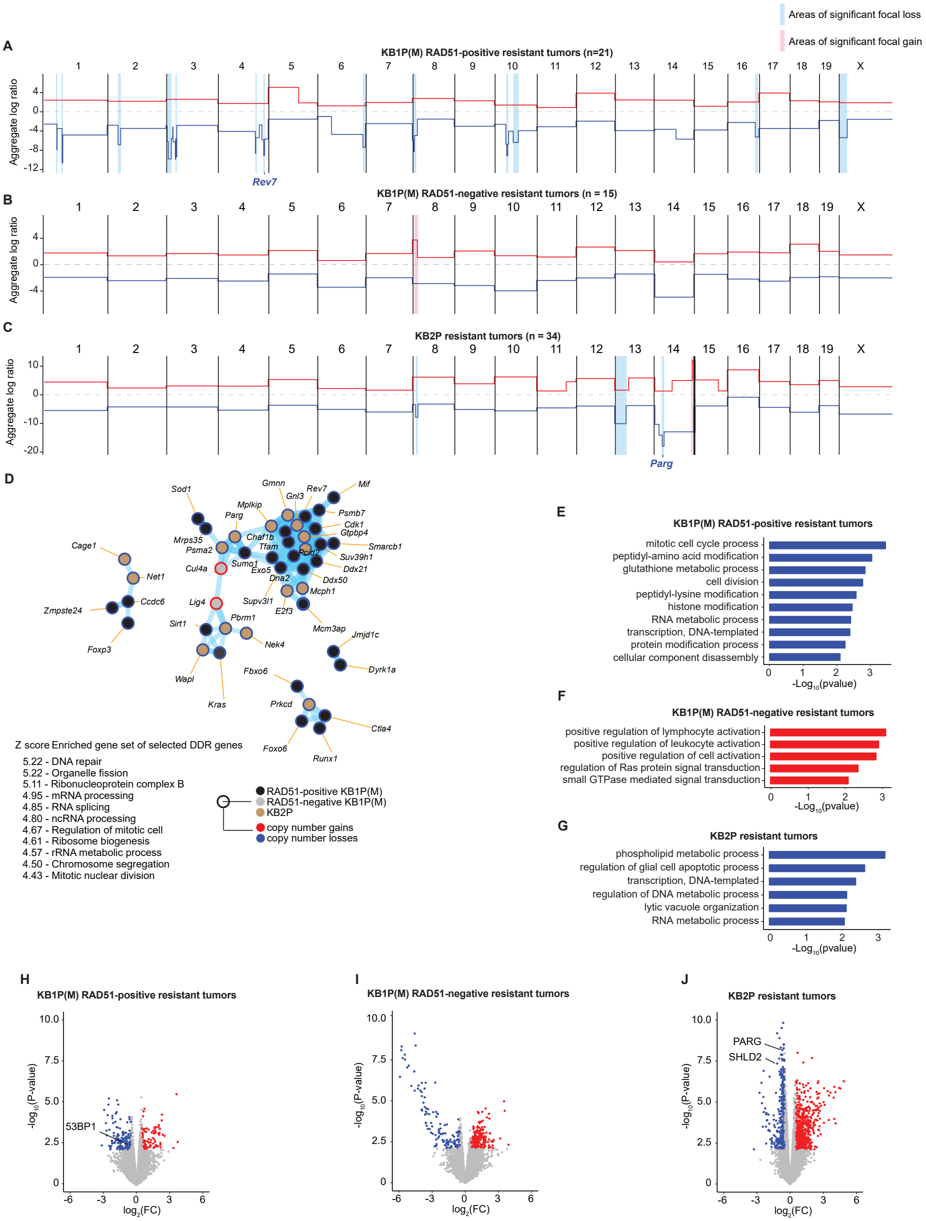

Supplementary figure 3 | Systematic analysis of genomic and transcriptomics data for PARP-naïve vs PARPi-resistant KB1P(M) and KB2P tumors. Related to figure 3. **A-C |** Identification of focal gains and losses in RAD51-positive (A), RAD51-negative (B) KB1P(M) resistant tumors, and KB2P resistant tumors (C) compared to matched naïve tumors using RUBIC[47]. Genes were highlighted if they are previously reported PARPi-resistance factors. **D |** Co-functionality network of DDR genes with significant focal gain or loss in RAD51-positive KB1P(M) (black), RAD51-negative KB1P(M) (gray) and KB2P (brown) resistant tumors. Gain (red) or loss (blue) are represented by border color DDR, DNA damage response. Top 10 pathways enriched by the genes in the network are listed with Z-transformed P value. The network construction and pathway analysis were performed by the GenetICA-Network[49]. **E-G |** Gene set analysis represented by the genes with significant focal gain or loss in PARPi-resistant RAD51-positive KB1P(M) (E), RAD51-negative KB1P(M) (F) and KB2P (G) tumors, detected by RUBIC. Because only focal losses were detected in RAD51-positive KB1P(M) resistant tumors, gene set analysis was performed for the genes with focal losses (blue). For RAD51-negative KB1P(M) resistant tumors, only one focal gain was detected, gene set analysis was therefore performed only for the genes with focal gain (red). KB2P tumors showed three focal losses and one focal gain. The focal gain only encoded mostly for non-protein-coding genes with the exception of three genes and thus gene set analysis was performed only for the genes encoded by the areas of focal losses. The gene sets with $P<0.01$ (fisher's exact test) were presented. **H-J |** Volcano plots of differentially expressed genes (DEGs) in PARPi-naïve vs PARPi-resistant RAD51-positive KB1P(M) (H), RAD51-negative KB1P(M) (I) and KB2P (J) tumors. Genes were highlighted if they are previously reported PARPi-resistance factors.

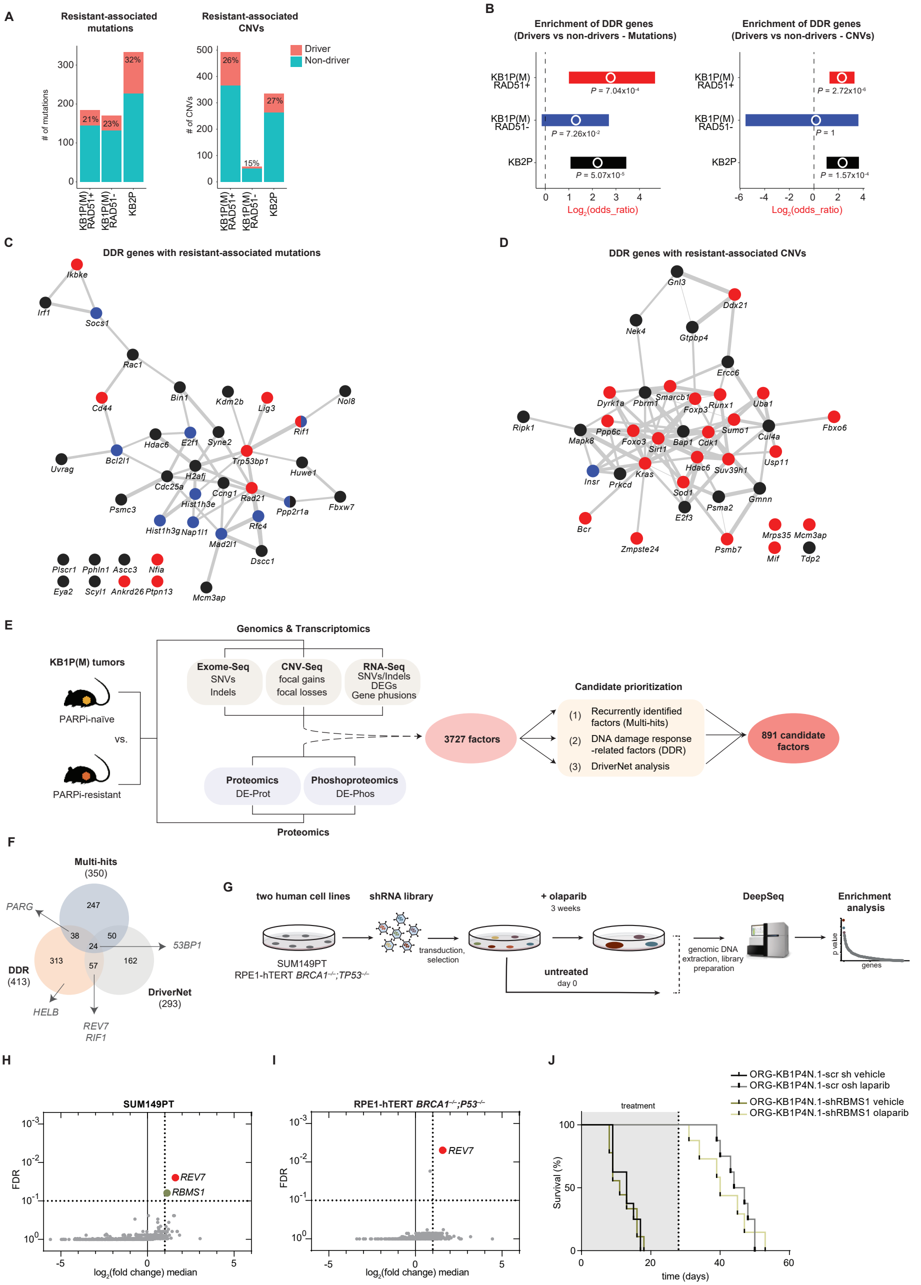

Supplementary figure 4 | In vitro loss-of-function screens fail to validate candidate drivers of in vivo PARPi resistance. Related to figure 4. **A |** Bar plot representing the number of driver and non-driver genes with high impact on expression of neighbors in a protein-protein interaction network. Driver potential was assessed for the genes with resistance-specific mutations (left) and copy number variations (right) by DriverNet[50]. **B |** Enrichment of DDR genes in the identified drivers from each resistant tumor group. Log2 odd ratios (proportion of DDR genes in driver genes vs non-driver genes) were presented with 95% confidence intervals. P-values were computed by fisher's exact test. **C-D |** DDR genes identified as drivers from resistance-associated mutations (C) and CNVs (D) were presented in the co-functionality networks. **E |** Schematic diagram showing the process of prioritizing candidate genes for functional screening. To enrich for plausible resistance driver genes, candidates were selected if (1) identified independently by at least two analyses ('multi-hits'), or (2) implicated in the DDR, or (3) identified as high-impact drivers in the protein-protein network using DriverNet[50]. The latter identifies genes which impact the expression of interacting partners or factors that share the same biological pathway and was used to correct for the fact that frequency analyses integrating data across different omic platforms ('multi-hits') fails to identify events restricted to one biochemical domain (e.g., mutation or phosphorylation), but nonetheless important for driving resistance 50. WE-seq, LCWG-seq and RNA-seq analysis was included for all tumor collections, including tumors whose RAD51-IRIF status was not determined in KB1P(M) (68 for resistant and 43 for naïve tumors), and proteomics and phosphoproteomics data was generated for some of the KB1P(M) tumors (12 for resistant and 12 for naïve tumors). **F |** Venn diagram representing the number of genes identified in candidate prioritization analysis. Genes were highlighted if they are previously reported PARPi-resistance factors. **G |** Outline of functional genetic enrichment screen. Screen was performed in SUM149PT and RPE1-hTERT *BRCA1*$^{-/-}$*;TP53*$^{-/-}$ cells. Surviving cells were collected after 3 weeks and analysis and hit selection was performed using the MaGECK algorithm (Li et al., 2014). **H-I |** Plot of distribution log2ratio (fold change (treated versus untreated)) median for all genes versus false discovery rate (FDR) for the screen carried out in SUM149PT (H) and in RPE1-hTERT *BRCA1*$^{-/-}$*;TP53*$^{-/-}$ (I) cells. **J |** Kaplan–Meier survival curves of mice transplanted with ORG-KB1P4N.1 tumoroids lines modified with indicated shRNA and treated with 100 mg/kg olaparib. End of treatment (28 days) is indicated by a dotted line.